ENERGY DISTRIBUTION OF SPUTTERED NEUTRAL ATOMS FROM A MULTILATER TARGET

Alan W. Bigelow, B.S., M.S.

Dissertation Prepared for the Degree of

DOCTOR OF PHILOSOPHY

UNIVERSITY OF NORTH TEXAS

August 2000

APPROVED:

Duncan L. Weathers, Major Professor
Samuel E. Matteson, Minor Professor and Chair of the Department of Physics
Jerome L. Duggan, Committee Member
Floyd D. McDaniel, Committee Member
C. Neal Tate, Dean of the Robert B. Toulouse School of Graduate Studies

Bigelow, Alan W., Energy Distribution of Sputtered Neutral Atoms from a Multilayer Target. Doctor of Philosophy (Physics), August 2000, 83 pp., 42 illustrations, references, 39 titles.

Energy distribution measurements of sputtered neutral particles contribute to the general knowledge of sputtering, a common technique for surface analysis. In this work emphasis was placed on the measurement of energy distribution of sputtered neutral atoms from different depths. The liquid Ga-In eutectic alloy as a sample target for this study was ideal due to an extreme concentration ratio gradient between the top two monolayers. In pursuing this study, the method of sputter-initiated resonance ionization spectroscopy (SIRIS) was utilized. SIRIS employs a pulsed ion beam to initiate sputtering and tunable dye lasers for resonance ionization. Observation of the energy distribution was achieved with a position-sensitive detector. The principle behind the detector's energy resolution is time of flight (TOF) spectroscopy. For this specific detector, programmed time intervals between the sputtering pulse at the target and the ionizing laser pulse provided information leading to the energy distribution of the secondary neutral particles. This experiment contributes data for energy distributions of sputtered neutral particles to the experimental database, required by theoretical models and computer simulations for the sputtering phenomenon.

ACKNOWLEDGMENTS

The professors in the Department of Physics at the University of North Texas provided excellent support and encouragement to me during my time at this institution. In particular, the professors in the Ion Beam Modification and Analysis Laboratory (IBMAL) gave me an opportunity to excel in the field of particle accelerator physics. To this regard, I thank Dr. Duncan L. Weathers, Dr. Samuel E. Matteson, Dr. Jerome L. Duggan, and Dr. Floyd D. McDaniel.

Completion of this work required assistance from several university support staff members. Electronics technicians, Dwight Maxon and Tom Schrimsher and machinists, Jim Cobb, Bobby Turner, and Ed Walter carried important roles during the development of the SIRIS apparatus. I am grateful for their pleasant camaraderie and for the unique mentor-apprentice training I received. University personnel were also very helpful with purchasing items and in countless other duties.

Former and current members of IBMAL were like an extended family. I thank all of them for the collective experience at UNT and for all the support and encouragement. Teamwork was a common trait among these colleagues and I valued all the collaboration and enlightening discussions that took place.

Finally, I must thank my immediate family. My mother, my father, my sister and by brother were consistent with their encouragement and compassion.

This material was based in part upon work supported by the Texas Advanced Research Program under grant no. 1997-003594-068.

TABLE OF CONTENTS

LIST OF ILLUSTRATIONS

CHAPTER 1

INTRODUCTION

When Grove investigated metal deposits on the inside of a gas discharge tube in 1853, the deposits were identified as electrode material and the door was opened to study the atomic collision processes between ions in the discharge gas and atoms in the electrodes (1). From Webster's Illustrated Dictionary, we learn that the verb "sputter" means "to speak rapidly ejecting saliva in small particles from the mouth" (2). Modifying only slightly this amusing term, sputtering now describes the event when an energetic particle impinges on a target's surface, resulting in the ejection of target components.

This study investigated sputtering behavior from a multilayered sample. Of particular interest were the energy distributions of sputtered particles. With the proper experimental apparatus, sputtering behavior measurements were made for atoms originating from one of two regimes in the sample.

Examples of several applications show how the sputtering phenomenon is beneficial in many areas. Material analysis techniques, such as secondary ion mass spectrometry (SIMS), employ sputtering to first remove matter from the sample. The semiconductor industry has chosen this material erosion method as a deposition process for thin films during device fabrication. When sensitive measurements are performed on a sample, a sputtering gun can remove surface contaminants prior to the experiment. Along with industrial use, examples of sputtering in nature are seen as the effects of the solar wind on the surfaces of meteorites and on planetary atmospheres. Since sputtering

processes are commonplace as in the examples above, the results reported herein can improve sputtering applications by increasing the understanding of the basic sputtering process.

Investigations into the sputtering process have occurred on three fronts. Theorists have identified several types of sputtering by elastic collisions. In the linear cascade regime, the process is often modeled as an incident ion initiating a series of binary collisions, a collision cascade that is then analyze using transport theory to predict energy redistribution among the constituents. Computer simulations apply binary collisions and molecular dynamics codes. As well, results from numerous experiments provide data to compare with the theory and the simulations.

Although much experimental and theoretical research has involved sputtering, some theoretical details of the sputtering process have yet to be resolved. One of these details is the energy distribution of sputtered neutral atoms. Theoretical models for the energy distribution of sputtered neutral atoms exist (3,4), but their results lack supportive experimental data. In addition, in a review of alloy and isotope sputtering by Sigmund and Lam (5), the survey list of important problems in the sputtering field included finding estimates of energy distributions of sputtered atoms from targets containing large composition gradients at the surface.

Atoms that are sputtered from the surface may have different energy distributions from atoms that originate from within a target. Those originating from within a material will initially require more energy than sputtered atoms originating from a material's surface in order to escape the surface. The additional energy could be attributed to the extra work required for an atom to reach the surface.

This work provides experimental results of the study of energy distributions of sputtered neutral atoms from different depths. While sputtering is a natural phenomenon and is such a common industrial technique, this work lends a greater understanding to how the sputtering process works as a whole. Also, these experimental results can boost theoretical development, which currently has shortcomings when applied to multilayer samples.

Liquid Ga-In eutectic alloy is an ideal target to study the energy distribution of sputtered neutral atoms. A previous study had shown that about 94% of the surface is covered with In in liquid Ga-In (16.5 at% In) eutectic and that the In enhancement is almost exclusive in the top monolayer (6). That study calculated the sputtering fraction from the first layer at 0.88 for a primary Argon ion beam energy of 25 keV. Using these values and considering constant In bulk concentration near 16%, one estimates that the fraction of In sputtered from the top layer is 0.96. Corresponding estimates also predict the fraction of sputtered Ga from beneath the top monolayer at 0.75. This target, therefore, suggests that the energy distribution from In is dominated by atoms sputtered from the surface. Likewise, any measurements of the energy distributions for Ga favor atoms sputtered from beneath the surface.

The Ga-In liquid target also eliminates the time dependence of sputtering. With a liquid target, as sputtering continues, vacancies are replenished due to the high atomic mobility and, consequently, the concentration gradient remains constant. This differs from the case of a solid target where time-dependent erosion takes place during the sputtering process.

This manuscript is divided into several chapters. The second chapter provides an overview of sputtering theory and sputtering simulations. The experimental apparatus that was designed for this study is described in Chapter Three. Results are presented in Chapter Four along with a discussion of comparisons to a simulation and to previous experimental angular distribution measurements. Chapter Five presents conclusions.

CHAPTER 2

THEORY

Predictions of sputtering behavior are possible using both analytical theory and computer simulations. This section includes a review of analytical sputtering theory and also investigates a molecular dynamics computer simulation technique.

Sputtering Theory for Multi-Component Targets

Four ion bombardment phenomena are summarized in a text on sputtering (7) for ions with energies of at least a few tens of eV. In one case, the incident ion may backscatter according to the kinematics of elastic collisions described by classical equations for conservation of energy and for conservation of momentum. In the case of sputtering, energy and momentum of the incident ion are transferred to target atoms, whereby ensuing atomic collisions may result in the ejection of target atoms from the surface. With ion implantation, the concentration of incident ions may increase at the end of their range; or, based on the chemistry between the implanted ions and the target atoms, these implanted particles may diffuse toward or away from the target surface. The text mentioned above also refers to electron and photon emission following ion bombardment; these secondary emissions enable other surface analysis techniques, such as Auger electron spectroscopy (AES) and particle-induced X-ray emission (PIXE).

Depending on the conditions of the incident ions, Sigmund discusses three theoretical models of collisional sputtering mechanisms (1). The *single knock-on model* describes the situation when an incident ion does not have enough energy to initiate a

collision cascade, yet certain individual target atoms are set in motion and can be sputtered. This model serves for incident ions with energies in the low to mid eV range and up to the low keV range for light ions. The *linear cascade model* depicts ensuing atomic collision cascades that can lead to sputtering. This regime assumes many moving particles, each colliding with only a stationary particle, and is valid for incident ion energies of keV up to MeV. The model for the *spike regime* describes the case where the incoming ion produces a high density of recoil atoms in motion; this model describes the case when the heaviest ions come to rest quickly in a target.

Sigmund has developed a comprehensive sputtering theory that is well documented in the literature (see, e.g. (2)). The sputtering yield is the number of sputtered particles per incident particle. In the theory proposed by Sigmund, there are four basic steps in calculating the sputtered yield. The first step involves obtaining the total energy deposited in the surface region by fast particles. Second, the initial deposited energy is transferred to late-generation recoil atoms. Third, the number of recoil atoms near the surface is determined. The fourth step isolates recoils near the surface with enough energy to overcome the surface binding forces.

For the 25 keV incident argon ions used in this work, the portion of Sigmund's theory that applies, the *linear cascade model*, is that which is based on the Thomas-Fermi model of atomic interaction. For this model, the screened Coulomb differential scattering cross section, a term for the number of scattered particles per incident particle on a target with a certain area density, N_s, is approximated by

$$d\sigma(E,T) = C_m E^{-m} T^{-1-m} dT \,, \tag{2.1}$$

with

$$C_m = \frac{\pi}{2}\lambda_m a^2 \left(\frac{M_1}{M_2}\right)^m \left(\frac{2Z_1 Z_2 e^2}{a}\right)^{2m}, \tag{2.2}$$

where E is the energy of the incident particle with mass, M_1, T is the energy transferred to a second particle with mass, M_2, m is a number between 0 and 1, C is a constant involving Thomas-Fermi screening radii, a, and atomic numbers, Z_1 and Z_2, and 8_m is a dimensionless function of m; 8_0=24.

The Thomas-Fermi potential holds for m=1/2 over most of the keV range and for m=1/3 when in the lower-keV to upper-eV region. At lower energies, if m is set close to zero, the cross section provides credible treatment for the Born-Mayer potential. In a linear cascade, most of the later atomic collisions occur in the eV energy regime. Hence m=0 will serve the linear cascade model applied to the experimental work in this study. This point is subtle but important because it treats the numerous collisions initiated by the higher energy of a primary impinging ion. With m=0, the differential cross section becomes a constant,

$$d\sigma(E,T) = 12\pi a^2 T^{-1} dT\,. \tag{2.3}$$

In this model, the *nuclear stopping cross section* for the incident ion is

$$S_n(E) = \frac{1}{1-m} C_m \gamma^{1-m} E^{1-2m}, \tag{2.4}$$

with

$$\gamma = \frac{4M_1 M_2}{(M_1 + M_2)^2}\,. \tag{2.5}$$

In developing a linear cascade theory, Sigmund applied the generalized Boltzmann transport equation to describe the motion of the target atoms (8). Previously, a

similar treatment had been applied in neutron transport theory. Developed from the kinetic theory of gas (9), the Boltzmann transport equation suits random media such as amorphous and liquid targets; however, it does not provide a complete description for monocrystalline materials. The common form of the Boltzmann equation used to solve for a distribution function $f(\vec{r},\vec{v},t)$ is

$$\left(\frac{\partial}{\partial t}+\vec{v}\cdot\nabla_r+\frac{\vec{k}}{m}\nabla_r\right)f(\vec{r},\vec{v},t)=\int K(\vec{v},\vec{v}_1;\vec{v}',\vec{v}'')d^3v_1d^3v'\,d^3v''\cdot\left|\vec{v}-\vec{v}_1\right|(f'f''-ff_1)\,, \tag{2.6}$$

where $f(\vec{r},\vec{v},t)d^3rd^3v$ is a statistical average over the number of atoms in a volume element d^3r at $\vec{r}$ moving with a velocity v in the range d^3v at time t;

$K(\vec{v},\vec{v}_1;\vec{v}',\vec{v}'')d^3v'\,d^3v''$ is the differential cross section for a projectile with initial velocity $\vec{v}$ and a target atom with initial velocity $\vec{v}_1$ to scatter each other into velocities $(\vec{v}',d^3v')$ and $(\vec{v}'',d^3v'')$, respectively; and $\vec{k}$ represents any external force acting on the incident particle. An important simplification used by Sigmund was to linearize this Boltzmann equation by limiting collisions to those between one moving and one stationary particle.

Also of interest is the expected number of atoms participating in a collision cascade. The expression for the mean number of atoms set in motion in a cascade with energies greater than some minimum, E_0, by an initial incident particle with even greater energy, E, is

$$n(E,E_0)=\Gamma_m\frac{E}{E_0}\,, \tag{2.7}$$

where Γ_m is a function that involves the mathematical gamma function. This mean number of atoms in a cascade is proportional to the incident particle energy as long as the energy is not absorbed by other phenomena. For the experimental work in this study, the proportion is $\Gamma_{m=0} = 0.608$.

Energy from the incident ion is, however, shared by collision cascades and by electronic excitation of target atoms. The amount of energy available for cascade initiation, $\nu(E)$, is reduced to the expression

$$\nu(E) = E - \eta(E), \tag{2.8}$$

where $\eta(E)$ is the energy absorbed through electronic excitation. With this expression, and following an argument for the isotropic distribution of atoms moving in the cascade in a solid angle $d^2\Omega_0$ about direction $\vec{\Omega}_0$, an expression was generated incorporating the recoil distribution in space due to an available energy distribution by an impinging particle, $F(E,\vec{\Omega},E_0,\vec{\Omega}_0,\vec{r})$:

$$F(E,\vec{\Omega},E_0,\vec{\Omega}_0,\vec{r})dE_0 d^2\Omega_0 d^3r \approx \Gamma_m \frac{F_D(E,\vec{\Omega},\vec{r})}{E_0^2} dE_0 \frac{d^2\Omega_0}{4\pi} d^3r, \tag{2.9}$$

where $\vec{\Omega}$ is the unit vector in the initial direction of motion for an ion starting its deceleration at $\vec{r} = 0$, and the density of deposited energy, $F_D(E,\vec{\Omega},\vec{r})$, stems from a conservation of energy expression,

$$\int d^3r F_D(E,\vec{\Omega},\vec{r}) = \nu(E). \tag{2.10}$$

When $F_D(E,\vec{\Omega},\vec{r})$ was integrated over an area, an expression for the depth profile of deposited energy was obtained:

$$F_D(E,\theta,x) \equiv \int_{-\infty}^{\infty} dy \int_{-\infty}^{\infty} dz F_D(E,\vec{\Omega},\vec{r}), \tag{2.11}$$

where the *x*-axis is normal to the target surface.

For a simplified mathematical treatment, Sigmund's theory consider particle flux in an infinite medium. The surface is then introduced into the infinite medium, and the evaluation of the number of particles intersecting this surface leads to an expression for the current density of target atoms. When integrated over the surface area, an equation for the outward current of target atoms is

$$J(E_0,\vec{\Omega}_0)dE_0 d^2\Omega_0 = \psi F_D(E,\theta,0)\cdot \frac{\Gamma_m dE_0}{E_0\left|dE_0/dx\right|}\left|\cos\theta_0\right|\frac{d^2\Omega_0}{4\pi}, \tag{2.12}$$

where ψ is the number of projectiles per unit time of initial energy, E, dE_0/dx is the energy loss of a particle moving through a random medium, and θ_0 is the particle ejection angle with the target normal.

When the above equation is integrated over E_0 and θ_0, a sputtering yield expression is found to be

$$Y = \Lambda F_D(E,\theta,0), \tag{2.13}$$

with

$$\Lambda = \frac{\Gamma_m}{2}\int \frac{dE_0}{E_0\left|dE_0/dx\right|}\int d(\cos\theta_0)\left|\cos\theta_0\right| P(E_0,\theta_0). \tag{2.14}$$

Here, $P(E_0,\theta_0)$ is introduced as the probability for an atom to escape the surface.

Subsequent steps incorporate the angular dependence of the particle escape probability, the term for the nuclear stopping cross section, the refraction effect of a particle passing through a planar potential step, and m=0. Sigmund's theory then gives

an expression for the differential sputtering yield with respect to energy and emission angle (the subscript, 1, denotes sputtered particle variables);

$$\frac{d^3Y}{dE_1 d^2\Omega_1} = F_D(E,\theta,0)\cdot\frac{\Gamma_m}{4\pi}\cdot\frac{1-m}{NC_m}\cdot\frac{E_1}{(E_1+U_0)^{3-2m}}\cdot|\cos\theta_1|. \tag{2.15}$$

In work on preferential sputtering from isotopic mixtures and alloys (10), Sigmund devised a sputtering yield expression for individual components of such targets,

$$Y_j(E',\vec{\Omega}') \cong \alpha_j\left(\frac{M}{M_j}\right)^m\left(\frac{Z_j}{Z}\right)^{b_m} f(Z_j)\,Y(E',\vec{\Omega}'). \tag{2.16}$$

Here, $''_j$ is the abundance of the j^{th} particle in the sample, b_m is a factor that includes m, and $f(Z_j)$ incorporates any chemical effects the j^{th} particle might have on the surface binding potential. M is a particle mass and Z is a particle atomic number. This expression is interesting because it provides a yield for a component of the target, $Y_j(E',\vec{\Omega}')$, based on the yield of a monoatomic target, $Y(E',\vec{\Omega}')$. Sigmund applies this expression to alloys in the case where the components have similar mass. Limiting assumptions for the two expressions above include target isotropy, meaning that particles in the collision cascade encounter the same conditions independent of their direction of motion.

Studies on preferential sputtering have also included models for surface layer composition changes (11,12). If a particular component on a target is preferentially sputtered, deficiencies in that component will develop in the region where it originated. Compositional changes continue until an equilibrium state is reached. This treatment does address target composition as a function of depth; however, it does not model well a sample that maintains its composition during particle bombardment.

The multilayer sample for this study is anisotropic and heterogeneous near the surface. It is also a liquid target that maintains its composition during ion bombardment. Theoretical approaches to the depth of origin of sputtered atoms have been limited to binary collisions in isotropic substances. In a review of sputtering depth of origin studies (13), a conclusive remark on the theory was made to the effect that while qualitative results are reached quickly for isotropic media, quantitative results require extensive details of the scattering process and that inaccurate results persist for multicomponent material. Therefore, more information on the nature of alloy sputtering is needed in order to build a theoretical framework to describe the case for multilayers.

Computer Simulations of Sputtering

When analytical theory falls short in depicting a complex problem, computer simulations may allow for comparison to experiment. Two principle types of computer simulation have been developed: molecular dynamics codes and those based on the binary-collision approximation.

First, molecular dynamics simulations model a sample of discrete atoms with interactive potentials and track the motions of all particles following each projectile impact. Molecular dynamics simulations of sputtering from liquid Ga-In targets were performed by Shapiro, Bengtson, and Tombrello (14). Their work involved setting up a target whose atoms were influenced by Gibbsian segregation and by attractive Morse potentials. A simulated melting process produced an appropriate eutectic alloy. For ion-atom interactions, Moliére potentials connected to the Morse potentials with cubic splines enabled repulsive cores necessary for scattering.

Results from these molecular dynamics simulations agree well with experimental results of angular distributions by Dumke et al. (15) and by Hubbard et al. (6,16) for sputtering from the same Ga-In eutectic. The simulation results encompassed first layer yields, mean starting depth, target temperature independence, energy distributions, polar angle distributions, and cluster emission. Energy distributions were compared to experimental work by Lill, but they did not agree. The energy distribution disagreement was attributed to the limitation in the sampling angles in the experiment compared to all angles considered in the simulation. However, reproducing the energy distributions over these limited angles can be used to check the experimental results by Lill. Finally, the simulation also includes polar angle distributions of the sputtered particles. Moreover, experimental results for the angular distribution of atoms sputtered from this material that were attained by Hubbard et. al. were fit to a power of the cosine function.

Monte-Carlo binary-collision models are also applicable to atomic collisions in the sputtering process. Such models treat collisions between isolated pairs of atoms, independent of potentials from neighboring atoms; the extensive monitoring of the sample atom motion used in the molecular dynamics approach is omitted. Although these models are less accurate than molecular dynamics simulations, Monte-Carlo simulations have reduced computational requirements and thereby can be performed on a personal computer.

The Transport of Ions in Matter (TRIM) code, included in the Stopping and Range of Ions in Matter (SRIM) (17) code package, is capable of sputtering simulation. These algorithms incorporate the binary collision approximation with screened potentials for a quantum mechanical treatment of ion-atom collisions. Also, they treat the target as

amorphous, conforming well to the conditions for liquid sputtering. Sputtering angular distributions obtained using the SRIM program for 25 keV Ar sputtering of liquid Ga-In eutectic have been compared with previous experimental results (18). The surface binding energy variable used in the simulation did affect the angular distribution comparisons. This is an important term needed to model the sample composition and it will need to be optimized prior to producing valid energy distributions in the future.

CHAPTER 3

EXPERIMENTAL METHODS

Overview

Sputter-initiated resonance ionization spectroscopy (SIRIS) is a technique for selectively analyzing materials through resonance ionization of secondary neutral atoms. SIRIS is a pulsed technique where a primary ion beam pulse initiates the sputtering process. Then, tuned lasers are used to resonantly excite and photoionize sputtered neutral atoms. Finally, these ionized particles, photoions, are accelerated towards an analyzing detector.

Surface and depth profile studies have widely employed SIMS as a measurement tool. SIRIS features encompass most of the benefits of SIMS along with heightened performance in the areas of efficiency, matrix dependence, isobaric and molecular interference, sensitivity, dynamic range, and quantitation accuracy (19). With probabilities for sputtered ions, $"^{+}$ and $"^{-}$, well below unity, the probability for sputtered neutrals $1-("^{+}+"^{-})$ is close to and can be considered unity (20). Therefore, by ionizing the neutrals and attracting them towards a detector, one can increase the sensitivity factor seen in other techniques that depend on sputtered ions such as secondary ion mass spectroscopy (SIMS). SIRIS measures the dominant component of the sputtered flux, the neutral particles. And, the resonant step in the ionization process makes the technique highly species selective. Considering these features, SIRIS is an ideal choice of technique for sputtering behavior studies.

Components of the SIRIS machine at the University of North Texas (UNT) include a low-energy particle accelerator providing a primary sputtering ion beam, a state-of-the-art target chamber, a tunable laser system for resonance ionization, and a position-sensitive detector. A time-of-flight process, initiated by a short start pulse of primary ions on the sample and terminated by a resonance ionization laser stop pulse at the entrance to the detector, permits velocity measurements of the resonantly ionized particles. Fast timing electronics and data acquisitions are handled through a virtual instrumentation software program. Details for each component of the sputter-initiated resonance ionization spectrometer are included in the subsequent sections. A schematic view of the SIRIS laboratory at UNT is shown in fig. 3.1. An exploded version of the detector region is shown in fig. 3.2 that represents the orientation of the sample used in this work.

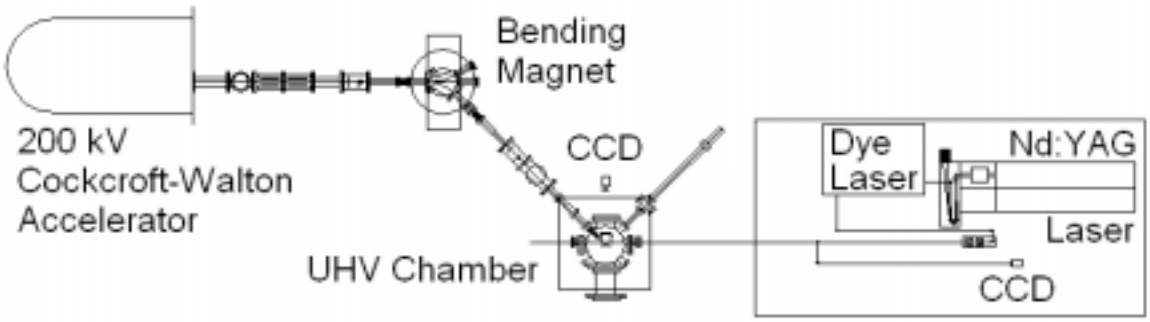

FIGURE 3.1. Schematic of the SIRIS apparatus. The sample, the position-sensitive detector, and the interaction region are inside the ultra-high vacuum (UHV) chamber.

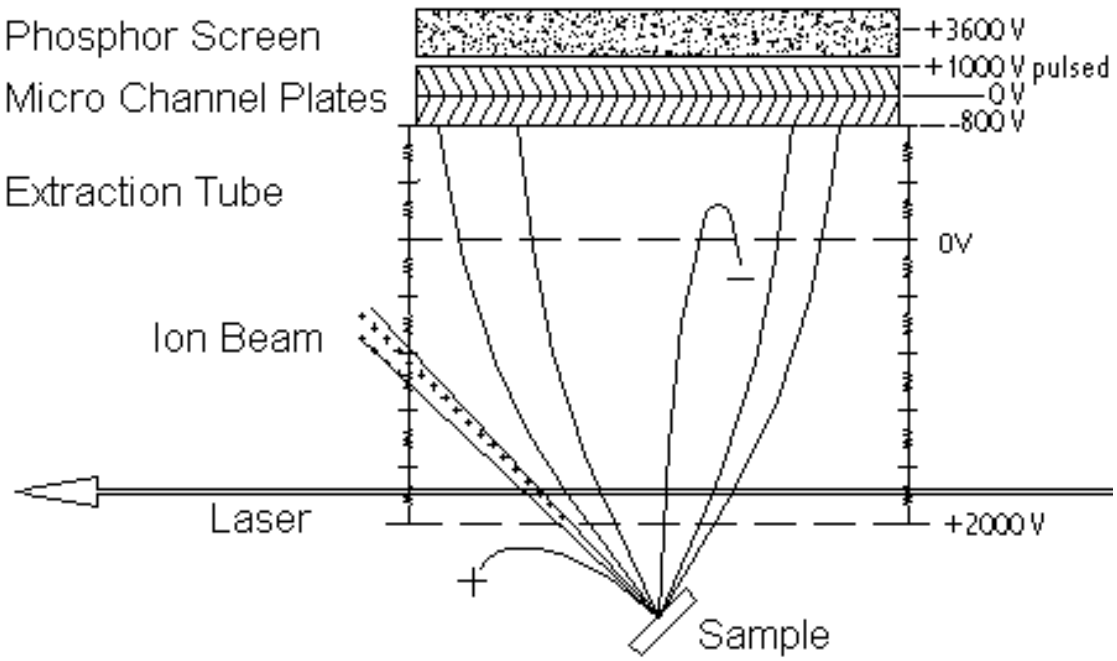

FIGURE 3.2. Schematic cross section of the interaction region and the position-sensitive detector. Dashed lines represent high-transmission grids.

Incident Ion Beam

SIRIS detects sputtered atoms, the yield of which depends on the total energy deposited in the sample. This study utilized a 25 keV pulsed Argon ion beam to initiate sputtering. Ion pulse widths were 200 ns and the system repetition rate was set at 10 Hz.

Argon was a convenient choice for primary ions to initiate sputtering because this element is easily ionized in the accelerator's RF ion source. A primary ion energy of 25 keV was used to enable comparisons to simulations of the sputtering energy distributions. The maximum magnetic field achievable in this bending magnet is about 1.2 Tesla. Ar ions of 25 keV require about half of the maximum magnetic field to pass through a 45 degree bending magnet with a 0.446 m radius of curvature. Particles-per-pulse estimates

are on the order of 10^5 for 200 ns pulses at typical D.C. ion beam currents of 100 nA. Under these beam conditions ions focussed on a $(100\ \mu m)^2$ area of sample produce a low fluence per pulse with, on average, one ion striking an area covered by 10^6 atoms during each pulse. These values are low enough so that a nominally high current does not lead to non-sputtering situations like blistering and evaporation.

Production of the primary ion beam used in this experiment begins with an ion source at the terminal of a 200 kV Cockcroft-Walton accelerator. Source gas enters a Pyrex gas bottle through a leak valve. A radio frequency (RF) oscillator with an approximate power delivery of 120 Watts at 60 megahertz ionizes these particles (21). Under the force of an applied extraction potential, the ions produced in the plasma state enter the accelerating tube. High voltage is supplied to the accelerating tube directly from a step up 1 KVA transformer. Resistively separated equipotential rings line the accelerating tube and supply the appropriate electrostatic gradient for acceleration of ions. When used without an insulating gas, the accelerator terminal voltage is limited to 100 kV.

After the acceleration stage, the ion beam successively passes through an electrostatic quadrupole doublet lens, collimating x- and y-slits, a 45 degree singly focussing analyzing magnet, a second set of slits, and a final focussing element. Water-cooled collimating slits were designed into the system to accommodate the maximum power delivery of the accelerator's ion beam. Tantalum slits were designed to dissipate up to 200 W of power, corresponding to a maximum ion current of 1 mA at 200 keV. For the same considerations, water-cooled Faraday cups were constructed to monitor ion beam currents. Photographs of both a slit assembly and a Faraday cup are in fig. 3.3.

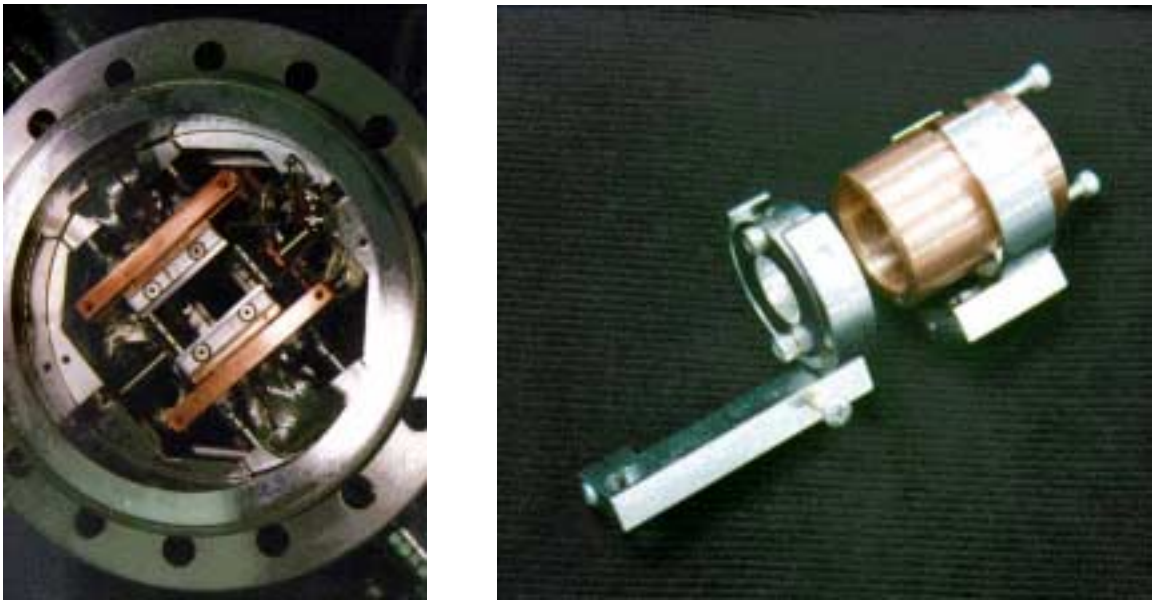

FIGURE 3.3. Photographs of ion beam slits and a Faraday cup assembly constructed for the SIRIS apparatus. Both components are water-cooled and are mounted in a four-inch housing.

Geometrical accommodations at the slits permitted ion beam pulsing by applying lateral electric field pulses across the first set of horizontal electrically isolated slits. While a 200V DC-offset, from a Kikusi Electronics Corporation Model PAB Regulated DC Power Supply, was applied to one slit side, the other slit received 200V pulses of 200 ns duration from an Avtech AVR-S2-PS Pulse Generator. During a pulse, the ion beam would pass through the slits along the ion optic axis. Otherwise, the DC-offset steered the ions away from an aperture placed further down the ion beam line.

Ion beam pulses were monitored with a current-to-voltage preamplifier with a 0.545V/mA conversion. At the output of the preamplifier, the voltage pulse was measured with either an oscilloscope or with a digital voltmeter. The ion pulse amplitudes were an important data-normalization factor in this experiment. In addition, this preamplifier

enabled an accurate determination of the ion beam energy through a time-of-flight technique. The time for the ion pulse to travel the known length of the beamline, from the first set of slits to the sample holder, was easily measured by monitoring the ion pulse arrival on an oscilloscope triggered by the ion pulse production.

Ion beam mass was analyzed with a sector magnet. For this system, a 45-degree singly focussing magnet selected ions with the appropriate momentum per charge ratio. After a study of the magnet's fringe field (22), shunts were introduced to shorten the effective magnetic field and to improve the magnet's focussing qualities.

The final focussing element was a custom-designed electrostatic quadrupole triplet lens with octupole excitation capabilities for spherical aberration control (23). Essentially, this final focussing element was necessary for point-to-point focussing and for a small, round beam requirement on the target to define the point of origin for the sputtered particles. A compression assembly of the quadrupole triplet lens provided means of spherical aberration control using a geometrical arrangement proposed by Matteson et al. (24). Pole dimensions were calculated using an ion optics treatment with transfer matrices. Figure 3.4 is a photograph of the final focussing lens element built by the SIRIS group.

From the object distance and image distance of the quadrupole triplet, it is estimated that the magnitude of the magnification, the image distance divided by the object distance, is one tenth. Object size is defined by the second set of ion beam slits; these vertical and the horizontal slit widths were held at 2 mm. Hence, the ion beam spot diameter on target was estimated to be 0.2 mm.

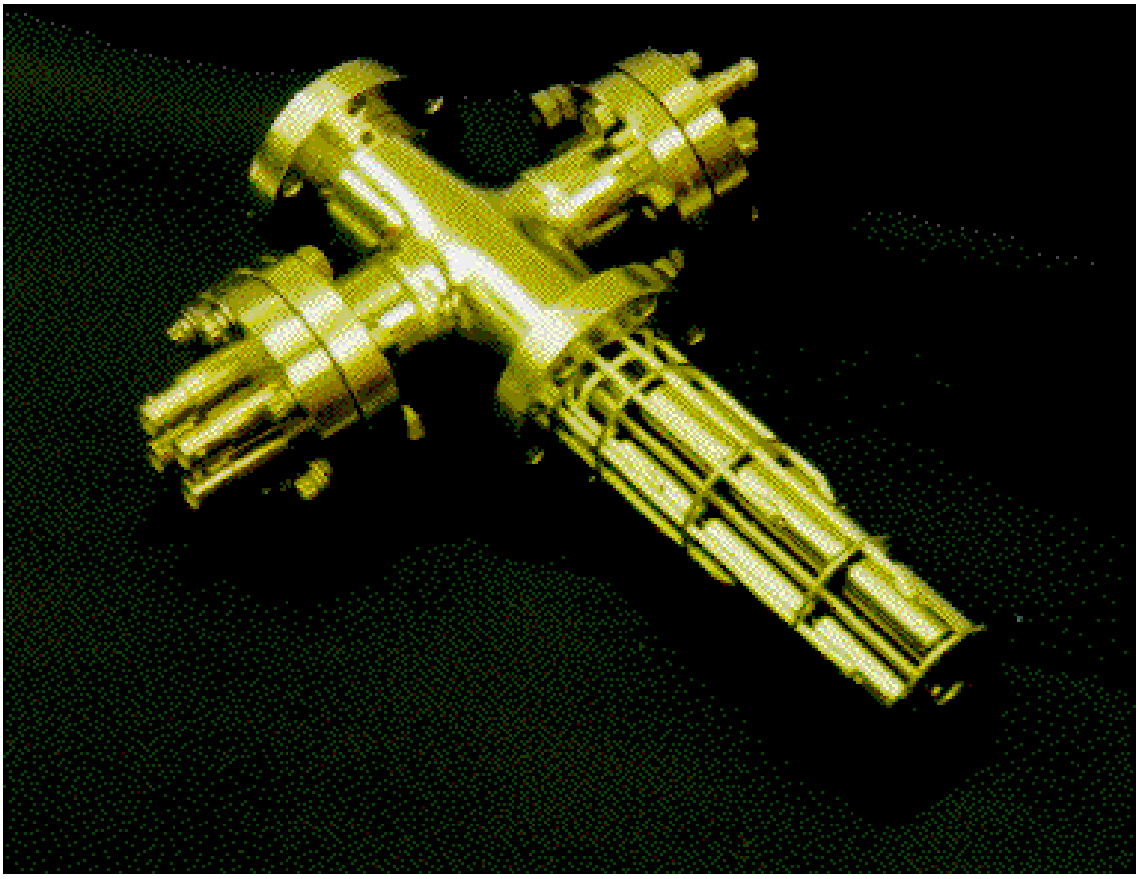

FIGURE 3.4. Photograph of the final focussing lens for the primary ion beam. The lens is an electrostatic quadrupole triplet.

Tunable Laser Beam

To electrically attract sputtered neutral atoms to a detector, the particles must first be ionized. Resonance ionization spectroscopy (RIS) is a technique for ionizing selected particles through multi-photon excitation schemes. For example, an excitation scheme that often works for selected elements is a two-photon process: the first photon produces a resonant excitation and the second photon produces ionization. Hence, a tunable laser system was essential for selective ionization of specific elemental species.

The description of the RIS process is complicated because it involves two competing features of light-matter interactions. Considering first the simple two-photon

excitation scheme, one observes that after a resonance excitation step occurs, the atom resides in an excited state. Subsequently, a second photon with sufficient energy can ionize the particle through a photoionization step. However, it is also likely that the second photon is identical to that used for the resonant step. In this case, the excited atom can experience stimulated emission and return to a ground state. This cycle can continue until a photoionization step occurs from the resonant state. Hence, the resonant state is considered to be a quasi-steady state. This feature and many other details of RIS are discussed in a seminal article by Hurst et al. (25)

Resonance ionization schemes exist for both Ga (26) and In (27). The Grotrian diagrams for Ga and In are shown in fig. 3.5 and 3.6, respectively. The wavelengths chosen for Ga ionization were 287.4 nm for the resonant step and 574.8 nm for the photoionization step. For ionization of In, the chosen wavelengths were 303.9 nm for the resonant step and 607.8 nm for the photoionization step. In both cases, the wavelength for the resonant step was the second harmonic of the wavelength for the photoionization step. These choices were convenient because, once the longer wavelength was produced by the tunable laser system, the shorter wavelength was obtained using a frequency doubling crystal.

Both In and Ga atoms have a doublet ground state. The higher state is a metastable state with a forbidden transition to the lower state. During the experiment, convenient RIS schemes were those that excited electrons from the lower state. Preferential sputtering behavior in energy or in angle was not expected for either doublet state of a particular element.

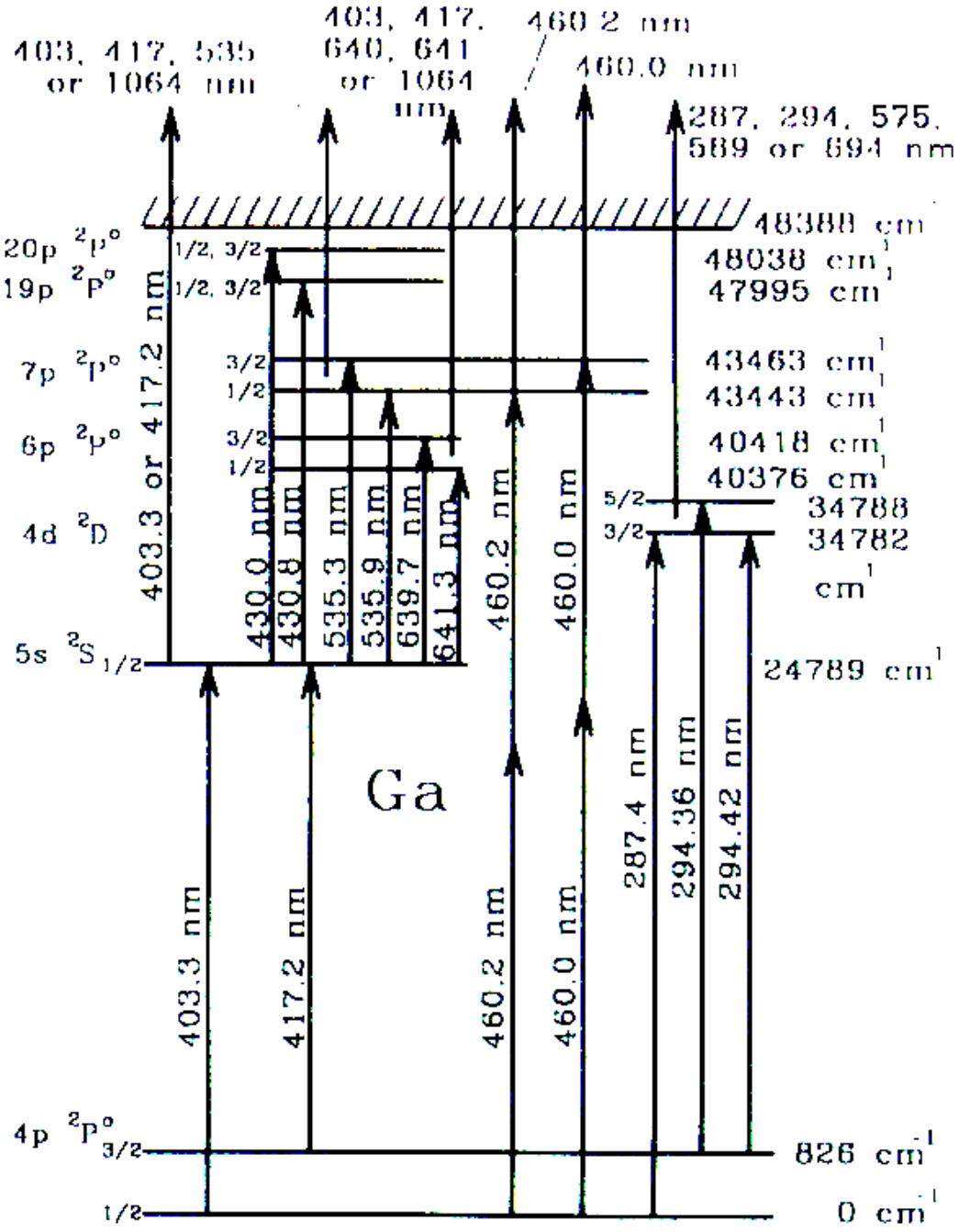

FIGURE 3.5. Grotrian diagram of resonance ionization spectroscopy schemes in Ga.

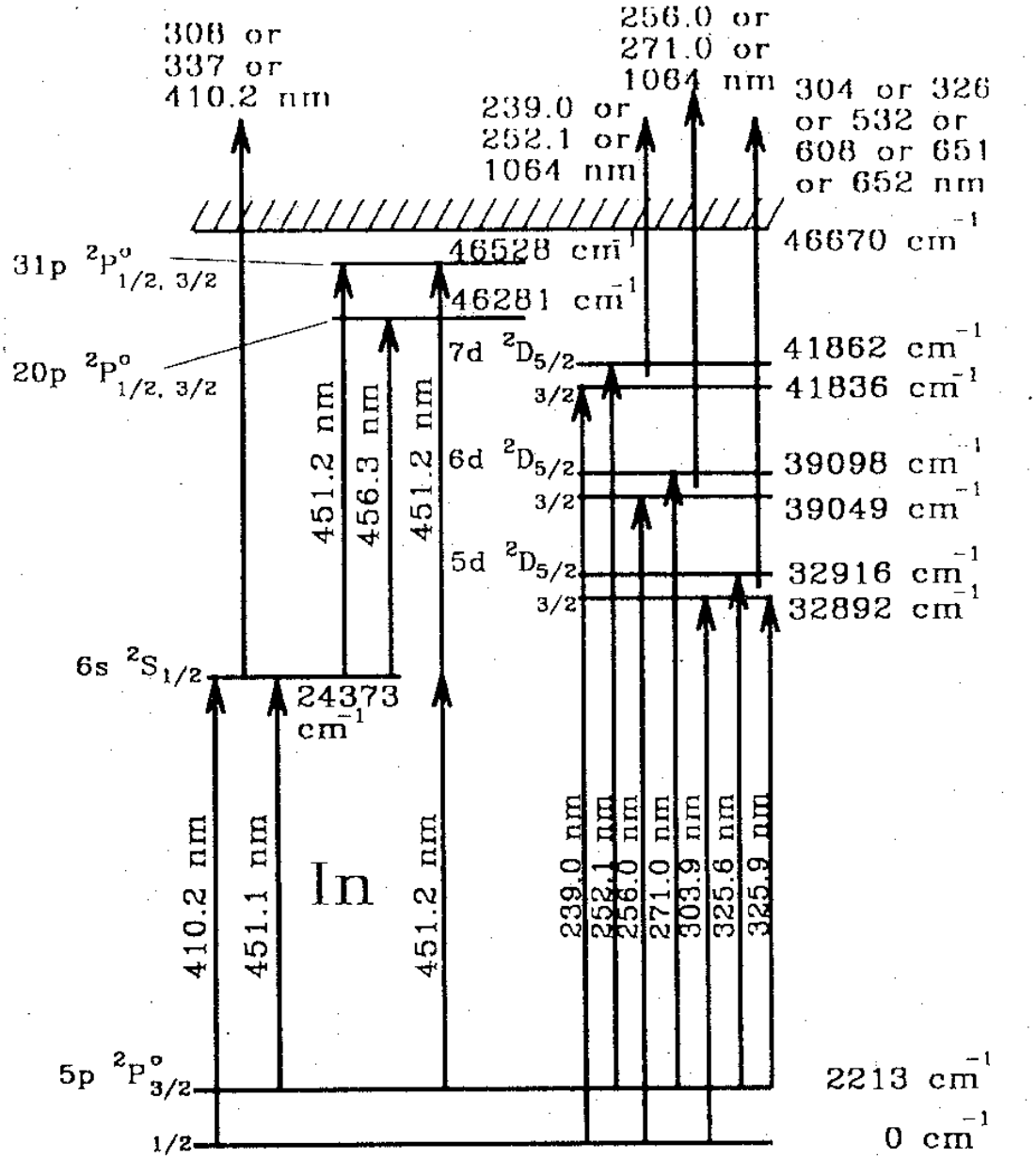

FIGURE 3.6. Grotrian diagram of resonance ionization spectroscopy schemes in In.

Laser systems comprised of a tunable dye laser pumped by a neodymium-doped yttrium aluminum garnet (Nd:YAG) laser are common for RIS use. Such a system was used in this experiment along with a non-linear frequency doubling crystal, b-Barium Borate (BBO). The laser light entered and exited the sample chamber through fused silica ports. A laser power meter placed on the exit side of the chamber monitored the average power for the incident laser pulses. Pump laser pulse widths were less than 10 ns and occurred ten times per second. The 10 Hz pump laser signal also initiated the timing sequence for the entire spectrometer.

One additional reason for choosing the resonance ionization schemes listed above was for the simplicity of producing those fundamental wavelengths using a dye laser. Both wavelengths of 574.8 nm and 607.8 nm can be produced with efficient, commercially available Rhodamine dyes. Lambdachrome laser dyes purchased from Lambda Physik for this experiment were Rhodamine 6G, Rhodamine B and Rhodamine 101. Three dyes were needed in order to obtain dye efficiency response curves centered about the desired wavelengths. One dye response curve may be chromatically shifted when combined with an adjacent dye of the same family (28). This technique was used to optimize both of the required fundamental wavelengths. The procedure for shifting the dye response curve to maximize laser power at 574.8 nm is shown in fig. 3.7. In addition to increasing the power output at a desired wavelength, this routine also improved the quality of the laser output by minimizing the spontaneous emission component that is inherent in dye lasers.

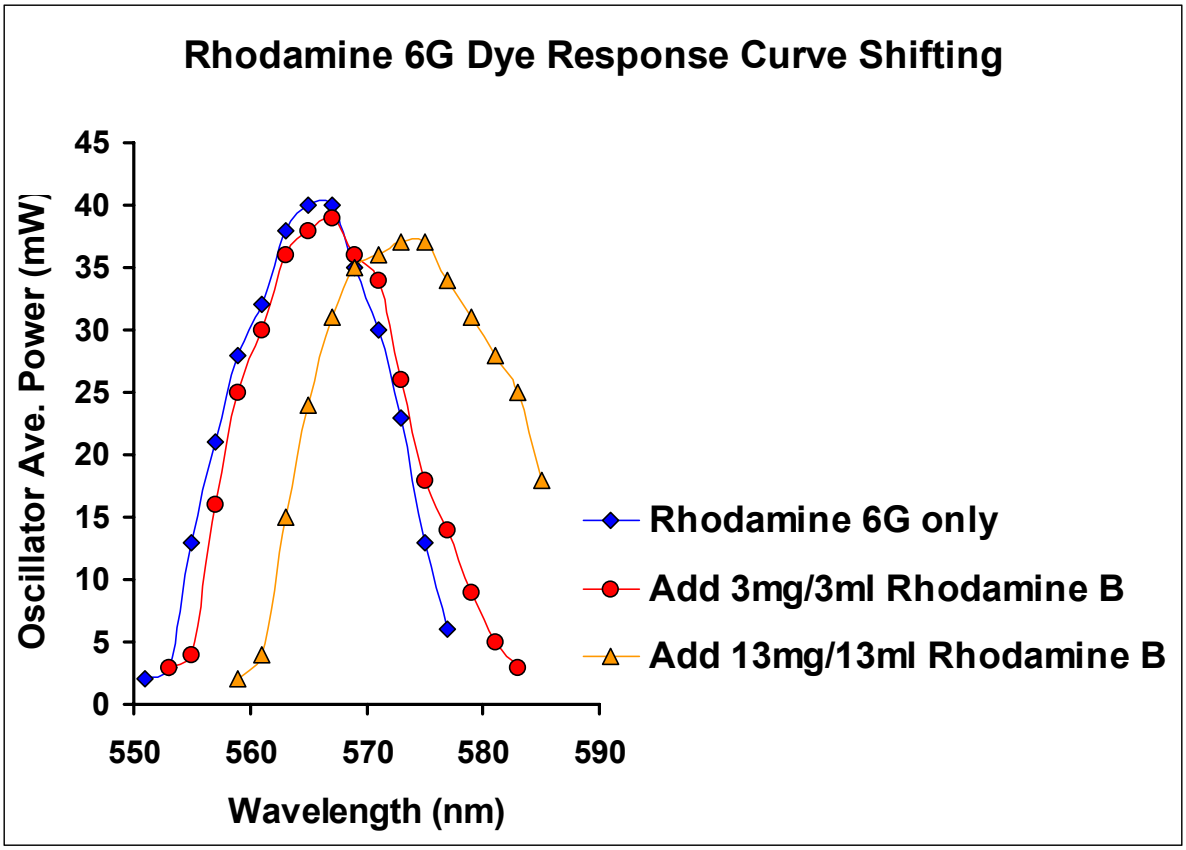

FIGURE 3.7. Laser dye response curve shifting by mixing adjacent dyes of the same family to maximize the power at 574.8 nm for RIS of Ga. These curves were measured using only the oscillator cell of the dye laser.

Two more laser beam features that needed attention were power and shape. The RIS schemes chosen for the experiment included power density values to saturate steps in the RIS process. Although it was not a necessity to saturate the RIS process, the laser beam average power was monitored throughout the experiment to maintain controlled ionization conditions and to provide a normalization factor, if necessary. In the case for Ga, RIS saturation conditions were consistently met. With RIS of In, laser power was such that ionization was linearly proportional to laser power and the data were normalized using the average laser power values.

Often, beam profiles from dye lasers were not simple to interpret. The liquid dye cell response and optics settings led to laser beam profile inconsistencies. These profile inconsistencies were most noticeable when the beam was directed through an attenuator placed in front of a charged-coupled device (CCD). Thus, razor-blade-collimating slits were placed just prior to the laser entrance into the UHV chamber. The desired effect was to narrow the width of the laser beam and to define its shape with diffraction. The slit width spacing was 0.015 inches (0.38 mm). With the wavelengths used and with the slit-to-target distance used, the diffraction pattern falls between that for Fresnel diffraction and that for Fraunhoffer diffraction (29). A Fresnel diffraction simulator, The Optics Project (TOP) (30), was used to approximate the laser width shape. Outputs from the Fresnel diffraction simulator are shown in fig. 3.8. The simulation provided merely qualitative beam profiles and did not compute diffracted beam widths.

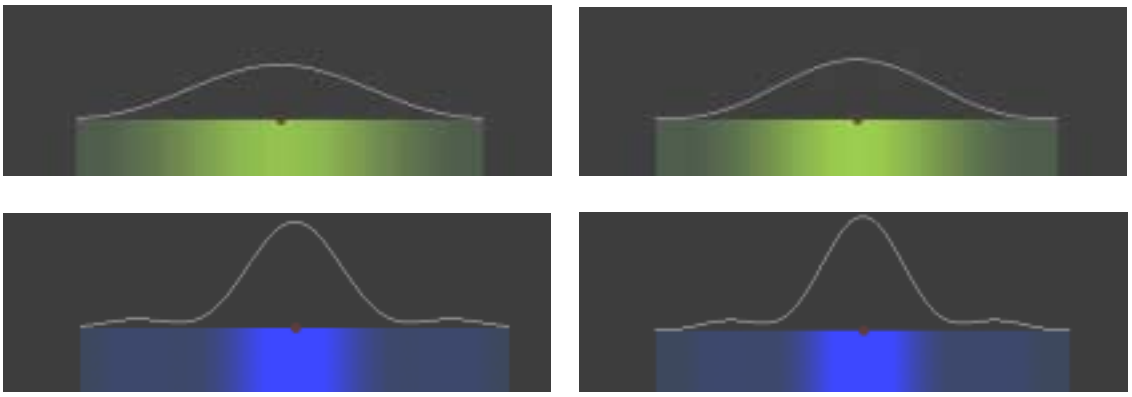

FIGURE 3.8. Fresnel diffraction simulation of laser beam intensity profiles produced by The Optics Project on-line interactive software. These simulations emulate the intensity profiles used in this experiment for RIS of Ga. At top, from left to right, the fundamental wavelength profile is presented for the near and far extents of the interaction region. At bottom, from left to right, the second harmonic profile is presented for the near and far extents of the interaction region.

Laser beam width size was calculated with standard equations for Fraunhoffer diffraction from a single slit. The sine of the diffraction half-angle, q, is

$$\sin\theta = \frac{\lambda}{a}, \tag{3.1}$$

where λ is the laser wavelength, and a is the slit width. The tangent of this same angle relates the laser beam half-width, $w/2$, at its distance from the single slit, D.

$$\tan\theta = \frac{w/2}{D} \tag{3.2}$$

Under the small angle approximation,

$$\sin\theta \cong \theta \cong \tan\theta\ . \tag{3.3}$$

This brings together the earlier two relationships,

$$\frac{\lambda}{a} = \frac{w/2}{D}. \tag{3.4}$$

Solving for w, we obtain,

$$w = \frac{2D\lambda}{a}. \tag{3.5}$$

The interaction region for the two-color RIS schemes used for atoms in this experiment was limited to the portion of the laser beam profile that included both frequencies, the fundamental and the second harmonic. From the Fraunhoffer diffraction equation treatment, it is evident that the width of the second harmonic component is half that of the fundamental. Hence, the second harmonic width profile (the central half of the total laser beam width profile) encompassed the RIS region. With the wavelengths for RIS of Ga and In, diffraction effects produced an 11.7% $\Delta w/w$, where Δw was the difference between maximum and minimum laser beam widths throughout the RIS

region. The second harmonic beam widths at the center of the RIS region, 0.343 m from the slits, were calculated as 0.547 mm for the wavelength, 303.9 nm, and 0.517 mm for the wavelength, 287.4 nm. These were the RIS region widths at the center of the interaction regions for In and for Ga respectively. The boundaries of the second harmonic beam defined the edges of the RIS interaction region because laser beam power densities used exceeded the saturation requirements for the resonant step by more than four orders of magnitude for both ionization of Ga and of In.

Sample Chamber

Vacuum conditions are crucial when working with ion beams and when studying surfaces. When examining surfaces, ambient gas adsorption can be minimized if the sample chamber is kept at high vacuum. From Somorjai's text one finds that the flux of ambient atoms, F, is

$$F\left(\frac{atoms}{cm^2 \cdot s}\right) = 3.51x10^{22}\frac{P(torr)}{\sqrt{M(g/mole)T(K)}}, \tag{3.6}$$

where P is the pressure, M is the average molar weight of the ambient gas, and T is the temperature (31). This implies that at pressures near 10^{-9} torr, it generally takes one hour to accumulate one monolayer on the surface. This is the upper limit of ultra high vacuum (UHV). UHV conditions were achieved in the sample chamber during this experiment.

UHV is attainable in the sample chamber with a combination of pumps. Sorption pumps rough out the system before an ion pump takes over. Numerous ports on the chamber allow for primary ion beam entrance, sample introduction with a magnetic arm, sample manipulation, viewing, pressure monitoring, laser input, reverse view low energy electron diffraction (RVLEED), and the position-sensitive detector.

Of utmost concern in the sample holder design was sample alignment with the ion beam, laser beam, and the detector. Precision-machined features on the position-sensitive detector provided the dominant alignment mechanism. An aperture in the side of the position-sensitive detector acted as a physical guide for the ion beam. An electrically conductive indicator incorporated into the sample holder design allowed for proper sample positioning with respect to the detector. By adjusting the sample holder manipulator, reference points were established through sudden electrical continuity between the sample holder and features on the detector. A simple confirmation of the ion beam alignment with the sample was achieved by inspecting a solid sample after sputtering had occurred; erosion was visible at the center of the sample.

Both detector and sample alignment to the laser were achieved with a shadow imaging method. Machined laser feed-through slots in the detector would block the collimated laser beam when its lateral position was scanned to either horizontal slot edge. This technique offered reference points for laser positioning with respect to the detector. Sample alignment with the laser beam was achieved by running the sample holder up toward the laser until the average laser beam power dropped by half. This check was performed at several sample holder rotation positions to account for mechanical run-out.

With a long moment arm on the sample manipulator, there was an inherent run-out that had to be corrected. This was most important in acquiring an angular calibration for the sputtered particles. A physical block mounted on the target holder limited the sputtering direction towards the detector. This set-up, when rotated through the angles of interest, provided for a signal edge that was defined by the limiting angle. Without compensation to the manipulator run-out, the calibration would have been inaccurate.

First, it was necessary to understand the rotation motion of the sample. Circular edges on the sample holder shelves were crucial to this process because they conserve a radius from the sample position. Manipulator settings for the sputter flight distance to the laser were assessed by moving the shelf edge up to the laser beam until it blocked half of the beam intensity. Settings corresponding to rotation increments of five degrees were recorded. These settings are shown in the plot in fig. 3.9; the trend was obviously sinusoidal. Hence, the fit was accomplished with equations describing circular geometry.

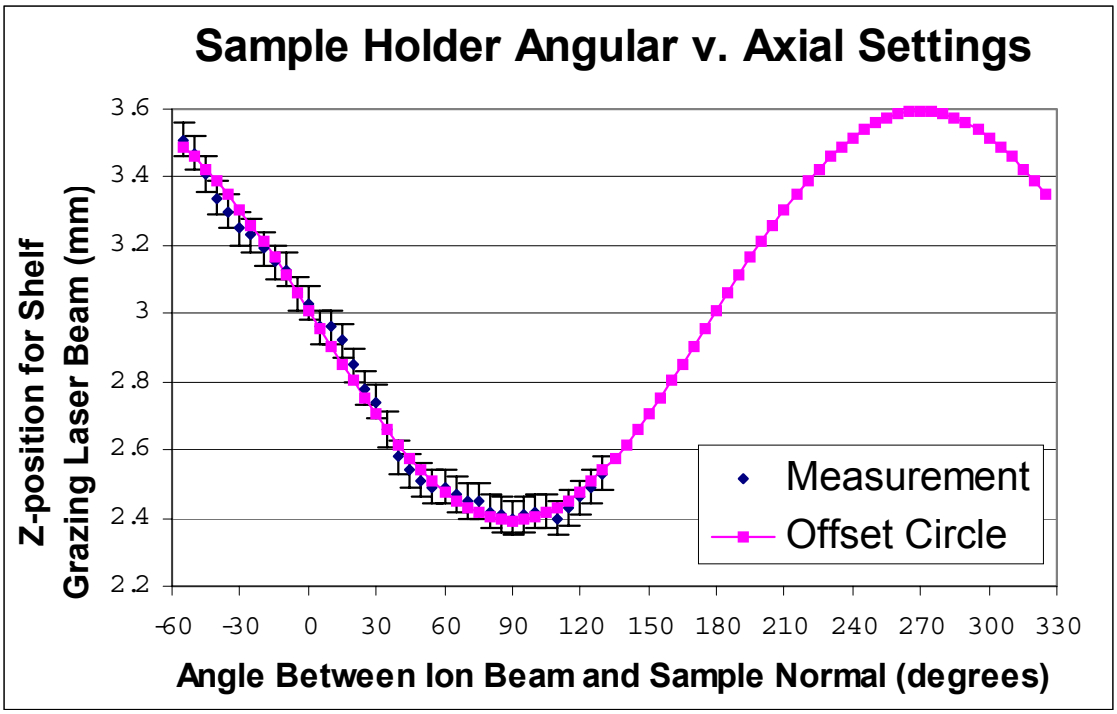

FIGURE 3.9. Plot to demonstrate sample holder run-out. Data values correspond to positions where the sample holder blocked half of the laser beam. Error bars on the measurements account for uncertainties due to total laser power variations.

Considering the trend in the z-position correction, a deductive approach led to predictions for correction in the x-position. At zero degrees in the above plot, the

sinusoidal curve passes through its equilibrium. This is one setting where the sample is set aside the rotation axis in only the x-direction. Following such observations, the x-position values were corrected with a sinusoidal treatment as well. Both axis corrections are plotted in fig. 3.10 as a function of manipulator rotation angle. It is not surprising that the run-out correction is accomplished with the sine and cosine functions in orthogonal directions.

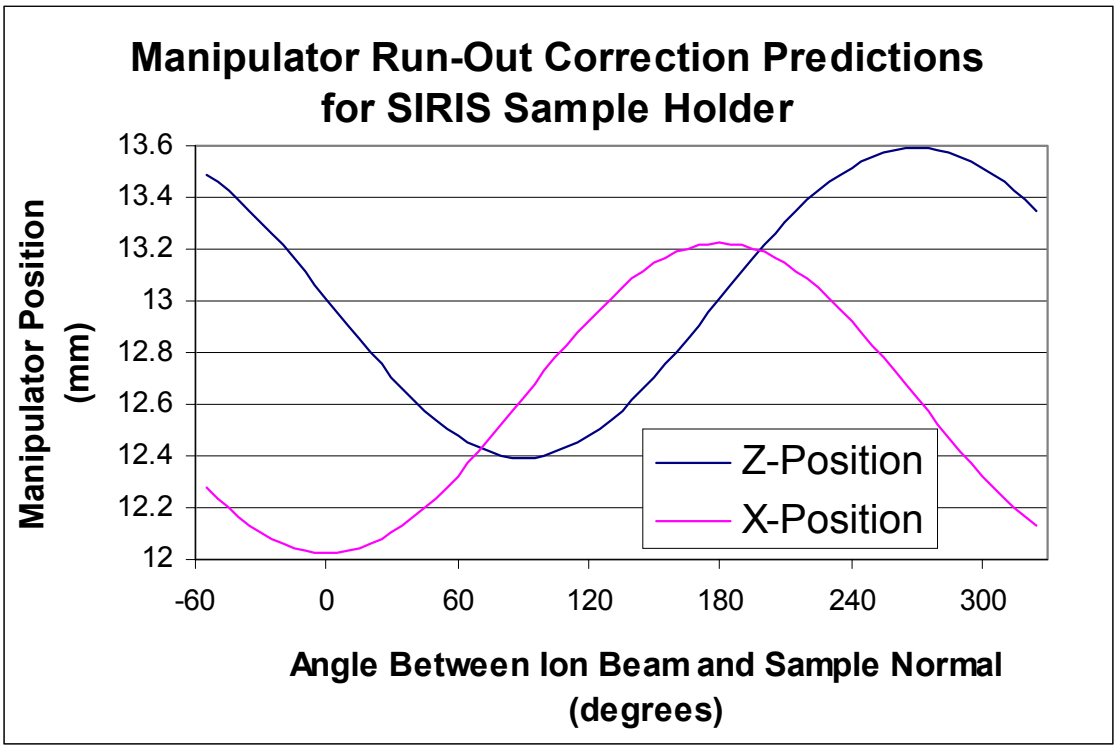

FIGURE 3.10. Sample holder correction to run-out for the manipulator x- and z-positions. The phase relationship pertains to manipulator positioning using the black scale markings.

Other considerations in the sample holder design were current monitoring and sample heating capabilities. The sample holder was electrically isolated; hence, it could be used as a Faraday cup to measure the primary ion beam current pulses. A radiatively

coupled NiCr resistive wire heater and a thermocouple were incorporated into the sample holder for temperature control. The sample holder is shown in fig. 3.11. And, fig. 3.12 is a view into the UHV chamber.

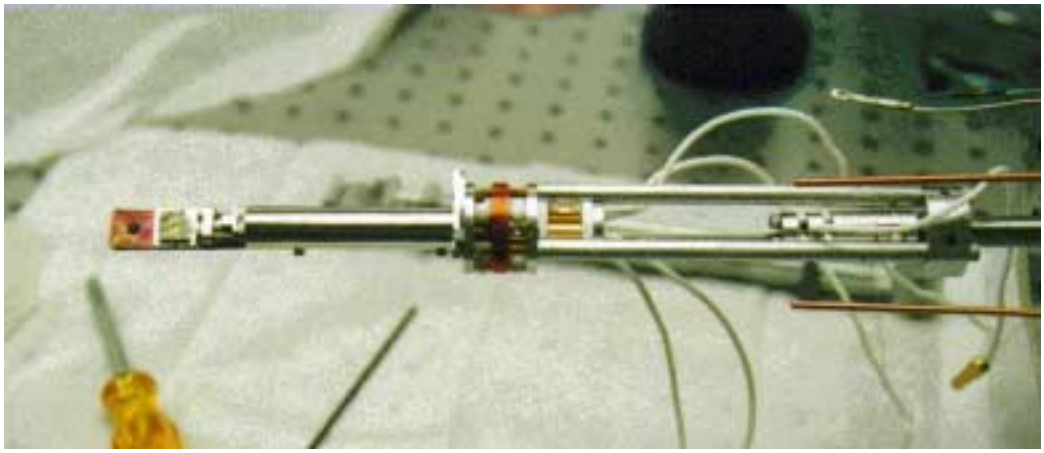

FIGURE 3.11. Photograph of the electrically isolated sample holder. Samples are mounted to the holder at the hole in the copper tip end on the left.

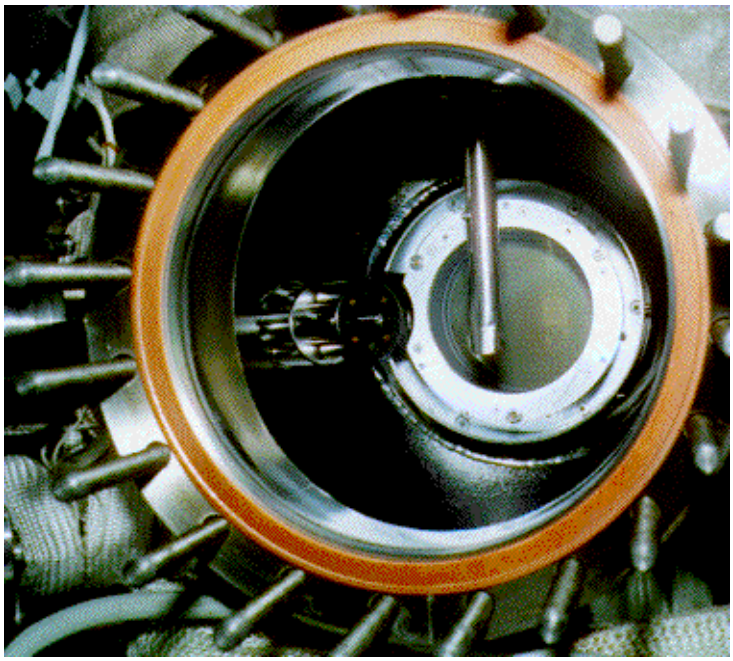

FIGURE 3.12. Photograph into the UHV chamber through the RVLEED port. The quadrupole triplet lens is at left, the sample holder drops from above, the position-sensitive detector is on the far side of the chamber.

Particle Detection

A position-sensitive detector that can resolve both energy and angle distributions of sputtered neutrals after ionization (32) was built in-house and provided the window for SIRIS measurements. Particle velocity was established by varying the time between sputtering and the subsequent ionization at a fixed distance from the target. And, the selectivity of resonance ionization establishes the particle mass. Together, particle kinetic energy of the sputtered neutral atoms is determined using the defining equation,

$$K.E. = \frac{1}{2}mv^2, \tag{3.7}$$

where *K.E.* is kinetic energy, *m* is mass, and *v* is velocity.

Particle detection succeeds the resonance ionization stage. A custom designed position-sensitive detector (33) accomplished this task. An applied electrostatic potential attracted the resonantly ionized particles to a pair of microchannel plates. The amplified signal then struck a phosphor screen leaving illuminated images to be captured by a Pegasus charged coupled device (CCD) camera connected to a computer. Emission angles of the sputtered neutral flux correlated with image positions after analysis.

Velocities for the resonantly ionized atoms were determined by TOF, where the path length was measured from the effluent origin to the laser interaction region and the flight time was the delay between the incident ion pulse and the laser pulse. Still, detection of the resonantly ionized particles was required. Design of a position-sensitive detector for the SIRIS system was modeled after the detector by Kobrin et al. (32). As a sputtered neutral particle left the sample's surface, it sequentially passed through a 95% transmitting grid and the laser interaction region. After ionization, the particle was

accelerated towards a second grid due to 2000 V applied between the two grids. Following the second grid, the particle continued acceleration toward Chevron paired microchannel plates (MCPs) that amplified the signal and illuminated a phosphor screen. The diameter of the microchannel plate assembly was 7.96 cm.

This detector design had the capability to accept sputtered atoms from a 90-degree range of angles. When the extraction potential between the grids was applied, the non-normal trajectories of the ionized atoms became parabolic with acceleration normal to the detector's surface. Energy and angle resolution depended greatly on the distance between the target surface and the laser interaction region. If the flight path increased, the energy of the atoms within the laser interaction region became more selective and angular resolution worsened. On the other hand, a shorter flight path increased angular resolution but decreased energy resolution. Since the initial ion pulse was 200 ns long, this was the limit of accuracy given to the time of flight.

Detector design optimizations by Li (33) estimated the best positions for the first grid, the ionization region, and the second grid. The first grid was 15 mm away from the sample's surface, the laser passed 20 mm from the surface, and the second grid was 80 mm away from the surface. Figure 3.13 is a photograph of the detector.

Position-to-emission angle calibration measurements were carried through three fronts. Experimentally, the aforementioned physical block, essentially a 0.8 cm tall limit in the horizontal plane, was used to limit sputtering emission angles to the sample normal. During the exercise, the ion beam impinged on the sample at the line intersection with the block. As the sample was rotated and corrected for run-out, resonance ionization

signal terminated at a detector position corresponding to the direction defined by the sample normal.

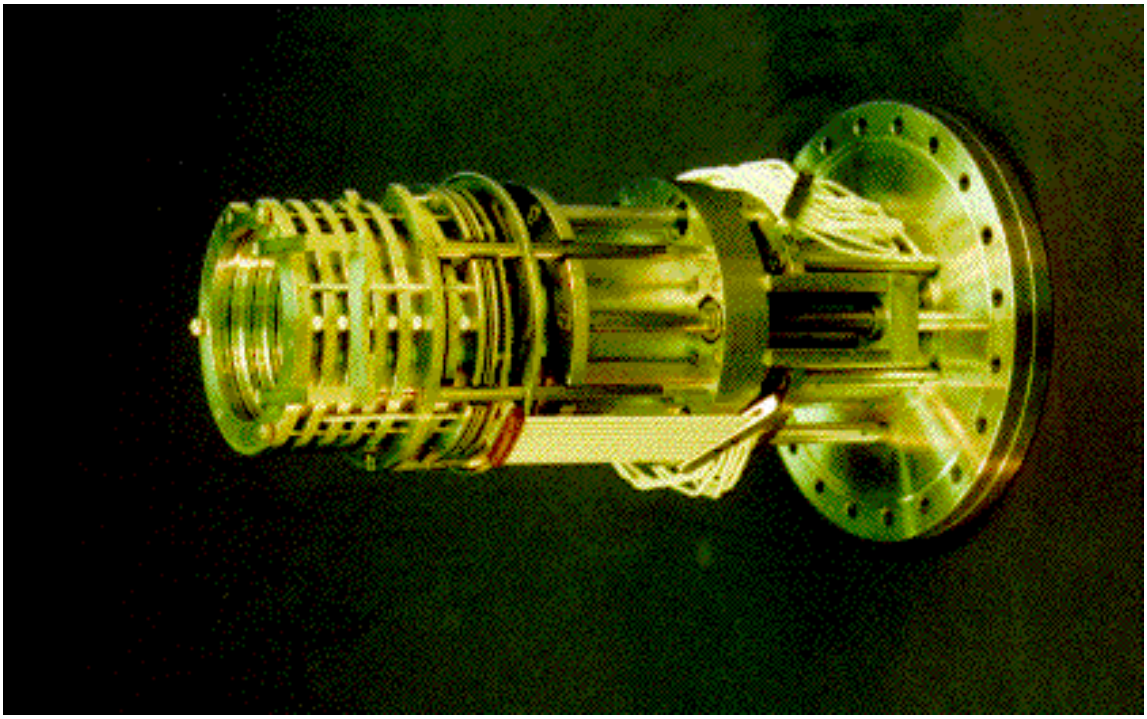

FIGURE 3.13. Photograph of the position-sensitive detector. From the left, the order of elements is acceleration tube, microchannel plates, phosphor screen, light tube, and 8 inch flange. Conductive leads individually pass through Alumina tubing and fish-spine beads.

Sputtered Ga from GaAs was used with a primary 30 keV Ar ion beam for these calibration trials. Energy settings of 1, 3, 5, 10, 15, and 20 eV were used with 5 degree incrementing limitations for the angle between the sample normal and the ion beam. The experimental trials took place up to the angle that defined sputtering emission parallel to the detector central axis. Up to this angle, the signal edge was defined by the particles with lowest energy. Beyond this angle, the test would have been hampered by higher energy particles effectively stretching the signal to the far side of the MCP. During the calibration test, a 650 ns ion beam pulse was used to increase the sputtered Ga signal, the

signal was only applied to the detector half close to the incident ion beam, and electric field symmetry was assumed inside the detector region.

Comparisons were made to the experimental calibration trials with results from the ion optics package, SIMION, and with a trajectory solution based on basic projectile motion equations. Figure 3.14 shows the comparison results for the 5 eV Ga setting. Good agreement was found at all energy settings. This good agreement allowed the analytical expression to be chosen as the conversion routine from detector position to sputtering angle. The expression used for this conversion was a solution to the projectile motion equations in two dimensions where acceleration was only applied to one dimension, the direction along the detector central axis. After eliminating the time element, the solution for obtaining the angles was

$$\tan\theta = \frac{dVx - 2DE_z - 2\sqrt{D^2E_z^2x^2 - dDVE_zx^2 + DVzE_zx^2}}{d^2V - 4DzE_z}. \tag{3.8}$$

With the dimension origin located at the sample, *z* was the perpendicular distance to the MCP and *d* was the position of the laser center. In addition, *x* was the image position on the MCP, *D* was the region under applied voltage, q was the sputtering ejection angle with respect to the detector central axis, E_z was the particle energy component along the detector central axis and V was the voltage applied to the detector.

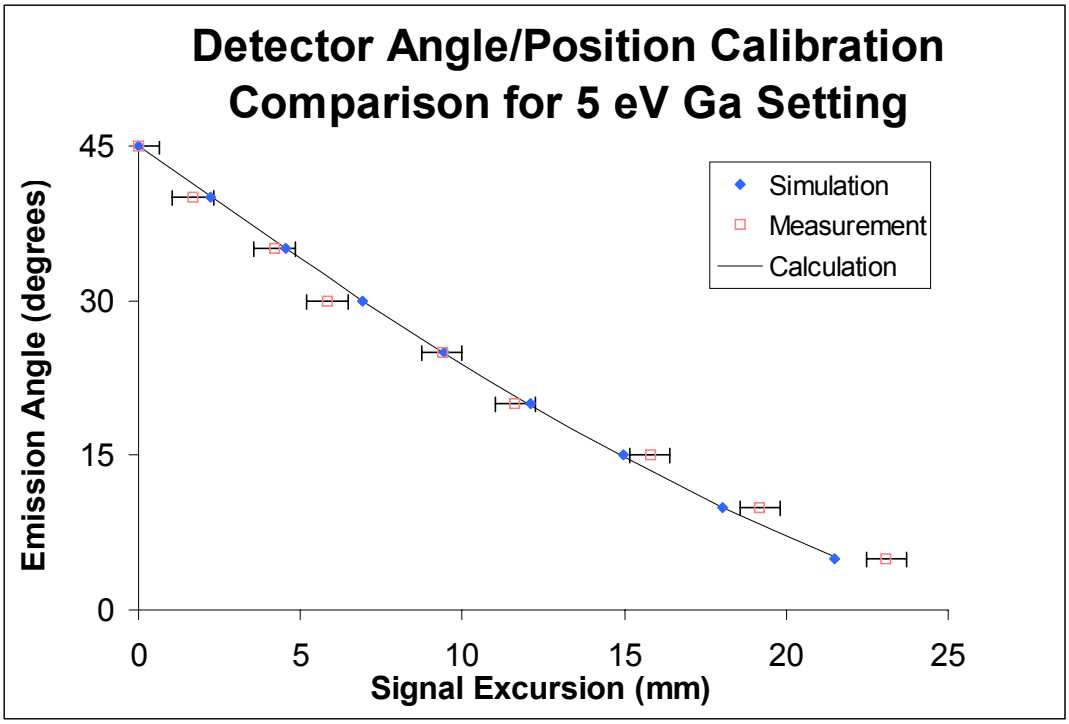

FIGURE 3.14. Experimental angular emission to detector impact position calibration measurements compared well with an ion optics simulation and with theoretical predictions. Error bars correspond to a ±5 pixel uncertainty in determining the calibration signal edge.

Virtual Instrumentation

As mentioned earlier, SIRIS is a pulsed system initiated from a 10 Hz Nd:YAG laser. Precision timing requirements demand automation. Hence, SIRIS control relies on virtual instrumentation. In this case, virtual instrumentation consists of a computer program linked to computer-automated measurement and control (CAMAC) modules which, in turn, are linked to the apparatus electronics. Features of the virtual instrument include experimental parameter control and data acquisition.

A user-friendly operator interface constructed using LabVIEW (34) software acts as a graphical virtual instrument base and is shown in fig. 3.15. LabVIEW is a graphical

programming environment for developing electronic instrument applications. The graphical program is symbolic as opposed to the traditional line-by-line text code and is more representative of a flow chart. Data flow occurs along virtual wires that connect the operations of the program. Mathematical operations are represented by graphical signal interconnects, and subroutines are represented by icons. Conventional *for* and *while* loops and case and sequence structures are available. An application program includes both a program diagram and a front panel. The front panel is designated as the user interface.

The SIRIS control program sequentially initialized the instruments, set the delay times, turned on the detector power supplies, cycled through the data acquisition stages, and turned off the detector power supplies. Other modes of operation were available that kept the power supplies on during a series of experiments.

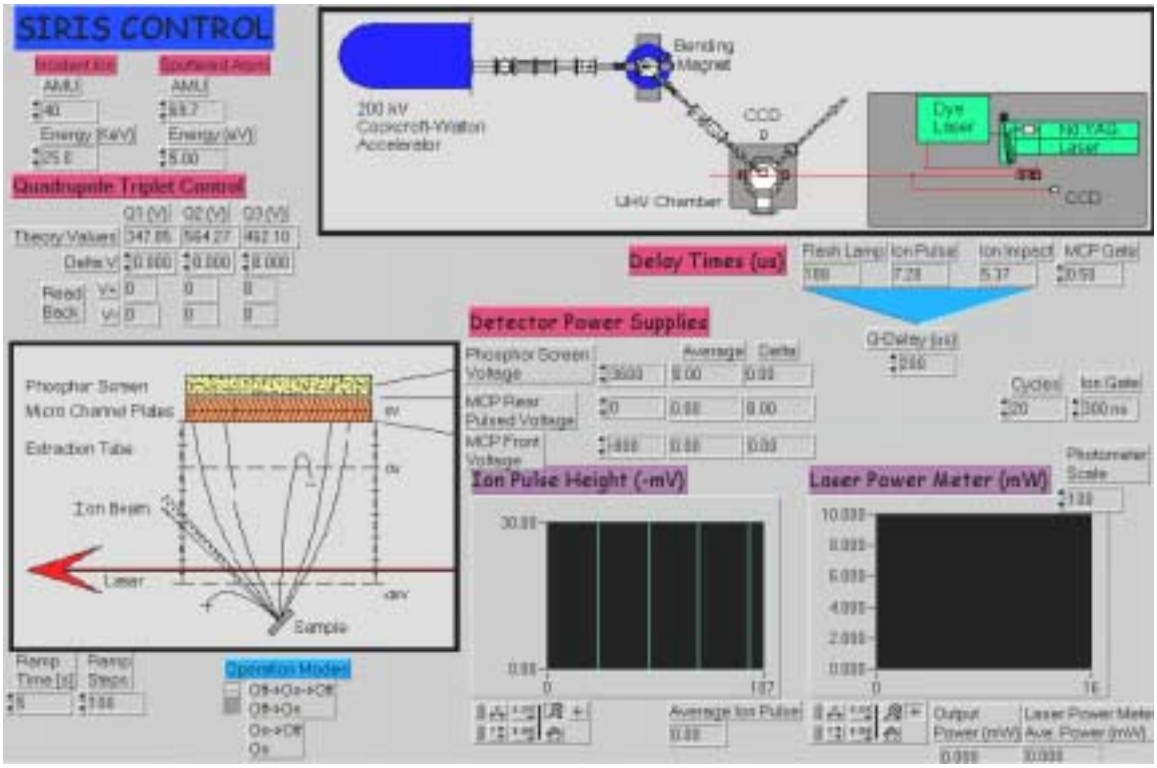

FIGURE 3.15. Virtual instrument control panel layout for SIRIS.

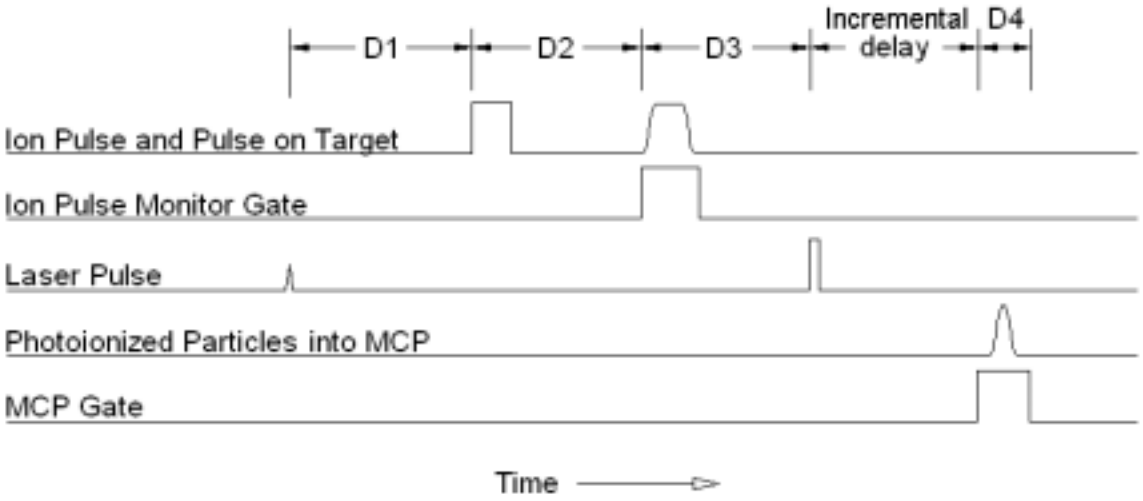

FIGURE 3.16. Pulse and event timeline for SIRIS. The detector extraction field was not pulsed.

Figure 3.16 is a graphical representation for the SIRIS pulse and event timeline where the delay times are represented by D1 through D4. The first three delay times always added up to 220 ms, the time interval between the Nd:YAG flashlamp pulse and the Q-switch trigger that delivered the greatest laser power. For example, if a 60 keV argon primary ion beam was used, typical values for these delays were: D1=214 ms, D2=4.6 ms, D3=1.5 ms, Incremental Delay=1.25 ms and D4=0.5 ms. D2 was the flight time for the primary ion beam pulse from ion beam deflector to sample. The time of flight for the sputtered neutral particles, D3, and the acceleration time to the detector for the resonantly ionized particles, Incremental Delay, were variable depending on the velocities of interest for the sputtered particles. D4 was the variable microchannel plate gate used to suppress noise from stray secondary ions.

Fast electronics control was possible through CAMAC modules whose crate was connected to a computer by a general purpose interface bus (GPIB) line. The electronics

diagram is shown in fig. 3.17. The system's timing chain, programmed into two LeCroy 2323A dual delay gate generators, received an initial start trigger from the Nd:YAG laser. An Ortec delay amplifier, model 427, was used as the incremental delay roughly corresponding to the acceleration time for the resonantly ionized particles through the detector. A gated LeCroy 2259B analog-to-digital converter registered the incident ion pulses. A DSP 2032 scanning digital voltmeter recorded the laser power meter voltages and the output from the high voltage power supplies applied to the quadrupole triplet and to the detector. Finally, a DSP 3016 16 channel digital-to-analog converter was used for remote control of the detector power supplies. Other SIRIS system components along the primary ion beam line such as valves, Faraday cups, and viewers could also be controlled through virtual instrumentation.

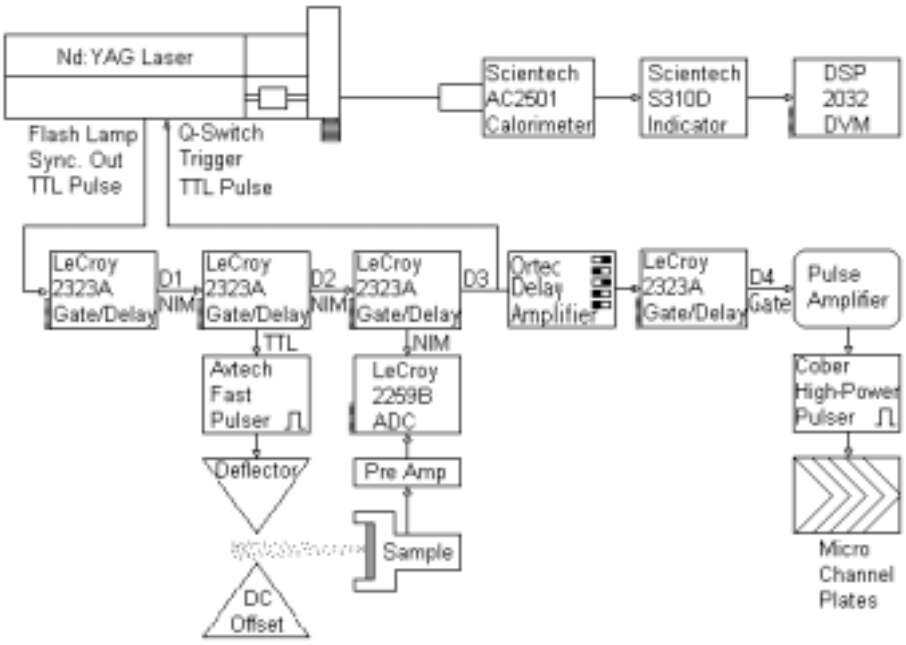

FIGURE 3.17. Timing electronics diagram for SIRIS. Peripheral hardware is also represented.

CHAPTER 4

RESULTS AND DISCUSSION

This chapter includes more specific experimental details as they pertained to the actual experiment. Starting with details on sample handling, the text presents data acquisition and data processing strategies. Following are analyses of error and comparisons to other simulations and experimental work involving the liquid Ga-In eutectic alloy.

Data Acquisition

Liquid phase Ga-In eutectic alloy sample material was obtained commercially. The handling of such samples has been previously documented (35). Two attributes of the target material, liquid Ga-In eutectic alloy, allowed for vertical mounting inside a vacuum system. In past experiments, the eutectic exhibited good wetting without dissolution to cobalt (36). This allowed vertical mounting of the liquid sample. In addition, the eutectic has a low vapor pressure, rated as essentially zero by the manufacturer (37); hence, it will not evaporate in a UHV environment. The sample was cleaned in a nitrogen back-filled glove bag attached to the sample introduction port. In this environment, the Ga oxide film layer that is known to form on the Ga-In eutectic (38) was swept off with a small wire brush. When the sample was placed vertically inside the sample chamber, a bulge developed in the lower region due to the sample's weight. Hence, during the experiment, the sample holder was adjusted so that the ion beam would retain approximately normal incidence in the vertical plane.

There were two possible approaches towards data acquisition in this experiment. On method would be to capture CCD images where individual ion impacts are distinguishable. The second plan involved integrating a CCD image over an extended time interval to capture an overall intensity distribution built from successive individual ion impacts. The decision to take the later approach hinged on the fact that longer integration would provide greater statistics and would require less processing time. Integration times used in this experiment accounted for 6,000 apparatus cycles each. Then three integration images were averaged together for each experimental parameter setting, accruing sputtering data from 18,000 single-shots. Precise individual ion impact positions could be recorded through compiling single-shot images, but, the complexity of handling 18,000 single images would only multiply during an experiment to measure the energy distribution of sputtered neutral particles. Examples of a single-shot image and a long integration are shown in fig. 4.1.

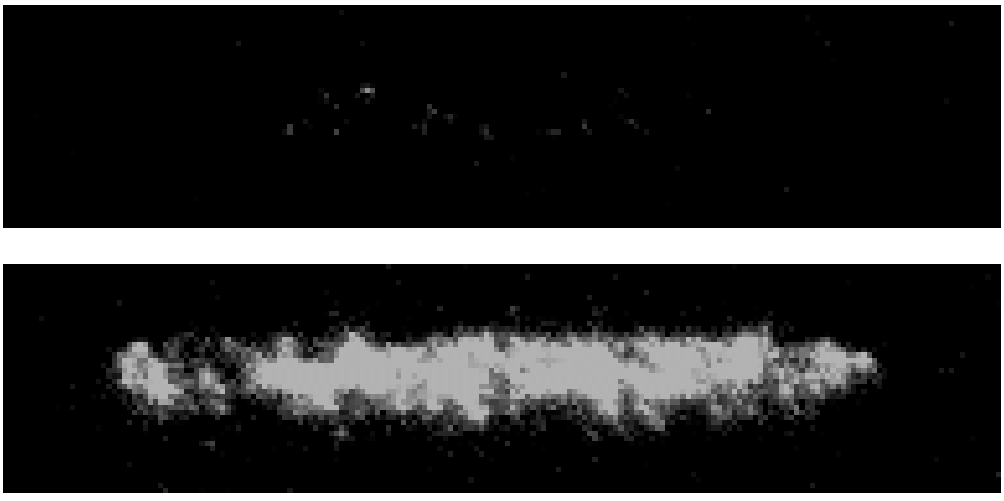

FIGURE 4.1. CCD images for a single shot, top, and for 400 cycles, bottom. Experimental conditions were for 100 ns pulses of 30 keV Ar on GaAs with RIS of Ga. The MCP gate time was 300 ns. These images were taken three days after the first SIRIS signal occurred; the apparatus was not yet at an optimal condition.

To complete an energy distribution of sputtered neutral atoms, a series of sputtered energy assignments were required. Each energy assignment was the component of particle energy in the direction normal to the face of the detector. For Ga, the energy series comprised 1, 3, 5, 7.5, 10, 12.5, 15, 20, 25, 30, 35, and 40 eV. For In, the chosen energies were 1, 3, 4, 5, 6, 7.5, 10, 15, and 20 eV. Differences in the energy range values used for Ga and for In were due to the differences in energy distributions for sputtered neutral atoms originating from a surface, In, and for those atoms sputtered predominantly from beneath a surface, Ga.

For each element, the primary sputtering ion beam was 25 keV Ar with 200 ns pulse widths. The amplitudes of the ion pulses and the average laser power were retained for data normalization. Typical instantaneous ion beam current was 100 nA and typical average laser power was 20 mW for Ga and 8 mW for In. In both cases, these laser power averages included a fundamental and a second harmonic wavelength. The BBO frequency doubling crystal was measured to have a 10% efficiency for second harmonic generation.

Data Processing

All ion impact positions on the CCD images were convolutions of particle energy and angle; image processing was required before final data of sputtered neutrals were available. For certain tests such as that for determining laser power dependencies for RIS, full image processing was not necessary. This test is described as an example of the direct information extraction from raw images. Explanation of the full data processing procedure continues later in the text.

Extracting pixel intensity values from the images first involved a conversion of file formats for all images. The Pegasus CCD camera software stored images with a FITS (.fts) format. These images were then transferred to TIFF (.tif) format using Avis Fits Viewer software, exporting to TIFF graytones. At that stage, it was important to use a histogram adjustment to linearly equalize all image intensities from one experiment. Then, the TIFF images were individually loaded into Global Lab Image software that had a convenient numerical extraction routine, the profile tool. Upon selecting a line, with variable thickness, across an image, a dynamic data exchange (DDE) feature sent the average pixel gray scale value across the line thickness to data columns in an Excel spreadsheet. With the sputtering image data, line thickness was set at 20 pixels and the lines spanned the entire horizontal of the image, 640 pixels. This region just about enveloped the signal height and conserved the pixel count across the image as a reference for ion impact positions on the detector.

Laser power dependencies for RIS were deduced from intensity values in these raw numerical data. Figure 4.2 shows an example of such data with a 6^{th} order polynomial fit for RIS of sputtered Ga. These Ga data were only normalized with the number of incident ions by dividing by the average ion pulse height. In fig. 4.3, a compilation of ionization intensity data fits is plotted for a variety of laser power values. For In, a similar compilation of intensity data fits is shown in fig. 4.4, but these data were also normalized for average laser power. The sixth-order polynomial fit for these types of data was deemed reasonable when statistical error of image intensity values converged for longer integration times.

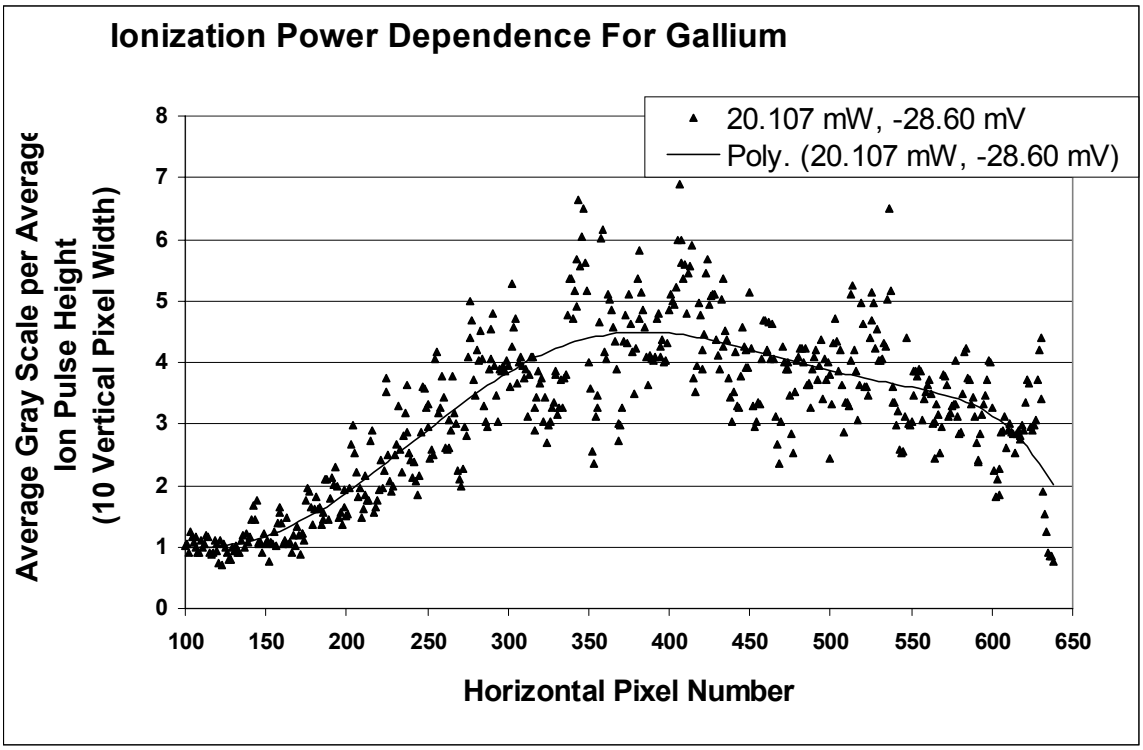

FIGURE 4.2. An example of SIRIS signal using a saturated RIS condition. This plot demonstrates a sixth order polynomial fit to the raw signal intensity values.

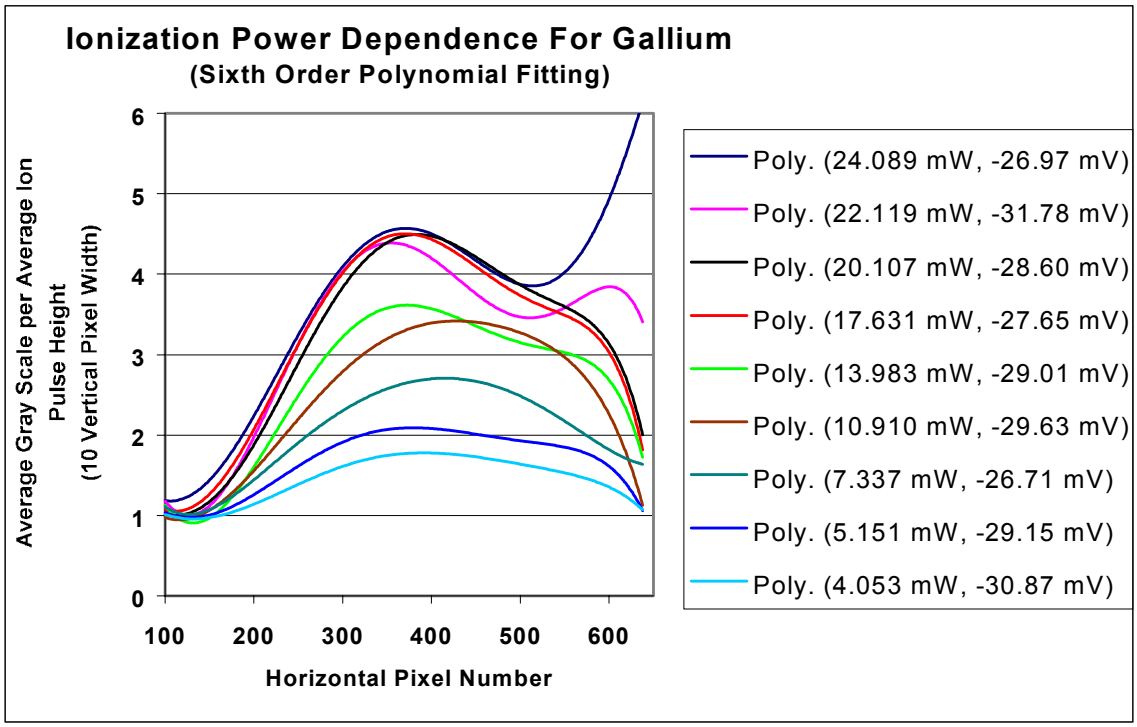

FIGURE 4.3. SIRIS signal intensity sixth order polynomial fitting, normalized with average ion pulse heights. As average laser power exceeded 17.631 mW, the RIS process for Ga was saturated. Note: a couple of the intensity profiles exhibited laser-initiated straylight background effects that effectively increased the signal intensity at the edge of the image. However, those images were still valid for this particular test.

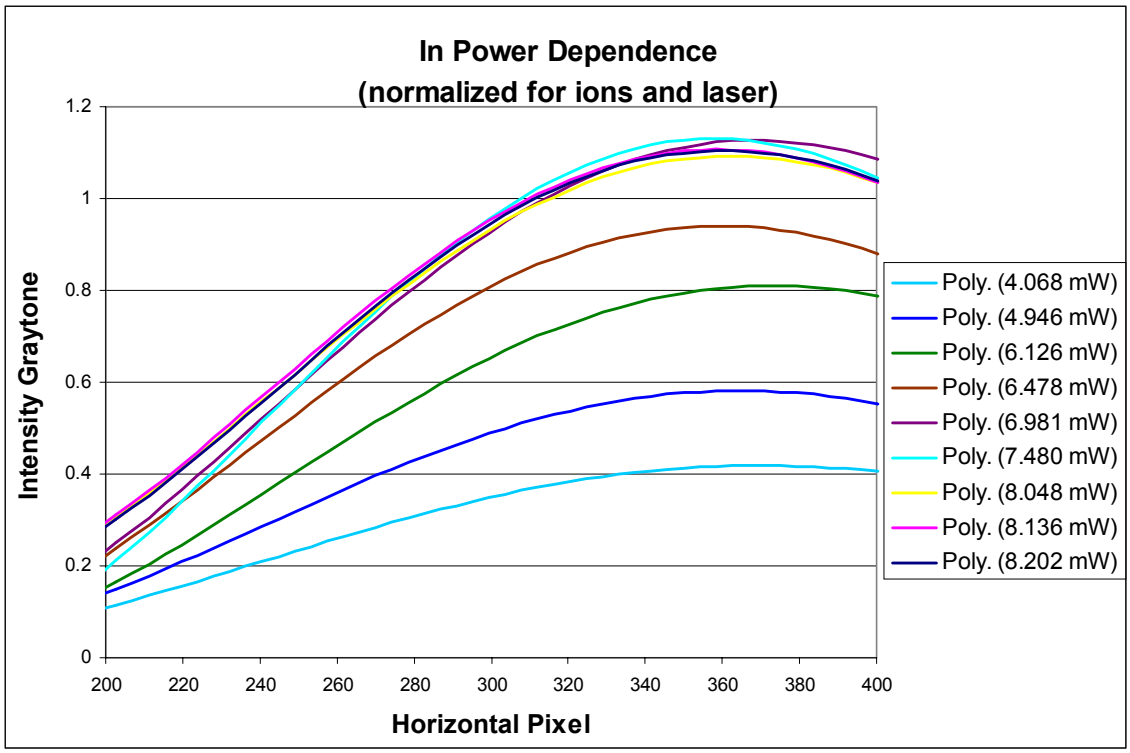

FIGURE 4.4. SIRIS signal intensity fits, normalized with average ion pulse heights and with average laser power. After average laser power reached 6.981 mW, the RIS process for In was linear with laser power.

These data for ionization power dependencies show that in the case of Ga, RIS saturation conditions existed for average laser power values above 17.631 mW. And for In, the ionization power dependency was linear with laser powers above 6.981 mW. During the experiment, data were acquired for Ga with RIS saturation conditions and for In within the RIS linear regime.

Correction to the response of the position-sensitive detector was necessary because the spatial efficiency of the MCP and Phosphor screen assembly was not uniform. The detector relative spatial efficiency was measured using an Am-241 radioactive alpha particle source centered at the front end of the detector. The alpha source is known to have isotropic emission due to the nature of radioactive decay. Only an inverse cubed radial correction was factored into the efficiency measurement to account for intensity variations for a planar intercept of emission from a point source. This inverse cubed factor was found from the mathematical ratio between the solid angle of the source to a differential area element on the plane intersecting the radial flux.

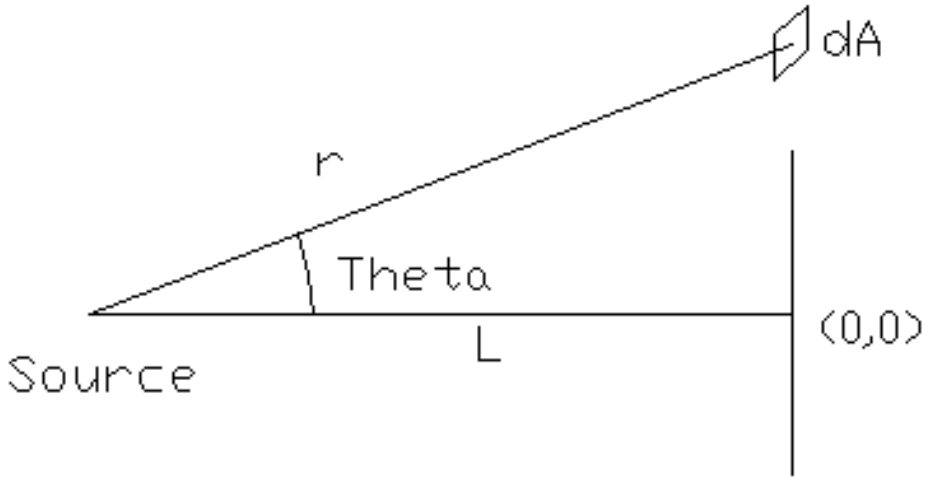

FIGURE 4.5. Diagram of an area element on a planar intercept of flux from a point source.

The mathematical treatment used to correct the efficiency measurement assumed an isotropic source and neglected electric field effects on the alpha particle trajectories. Refer to fig. 4.5 for a diagram pertaining to the following derivation. Variables used in the treatment were the number of alpha-producing decays per second, n_s, the perpendicular distance from source to MCP, L, the angle between alpha trajectory and detector normal, q, the particles per steradian per second, $I_0=n_s/(4p)$, and the infinitessimal increment of area, *dA*, on the MCP face. Cartesian x-coordinates were implemented at the MCP face, where the origin was set at the plane intersection with *L* and the midplane of interest is at *y*=0. Spherical coordinates were used to describe the radial trajectory of alpha particles from the source. The projection of *dA* onto a plane normal to the radial emission from the source was *dA*cosq. The solid angle of *dA* as seen from the source was *d*W(q).

$$\frac{d\Omega}{4\pi} = \frac{dA \cdot \cos\theta}{4\pi r^2}, \tag{4.1}$$

where *r*=*L*/cosq. The solution for *d*W was

$$d\Omega = \frac{dA}{L^2}\cos^3\theta\ . \tag{4.2}$$

Theoretical intensity at (x,y) on the MCP face was

$$I(x,y) = I_0\frac{d\Omega(\theta)}{dA} = I_0\frac{\cos^3\theta}{L^2}, \tag{4.3}$$

where

$$\cos\theta = \frac{L}{\sqrt{L^2+x^2+y^2}}\ . \tag{4.4}$$

After substitution,

$$I(x,y) = \frac{n_s}{4\pi} \cdot \frac{L}{(L^2 + x^2 + y^2)^{3/2}} . \tag{4.5}$$

Along the midplane (y=0), this simplified to

$$I(x,0) = \frac{n_s}{4\pi} \cdot \frac{L}{(L^2 + x^2)^{3/2}} . \tag{4.6}$$

It was found that the y-contribution to this term was negligible under the experimental dimensions. Hence, normalization of the intensities for spatial efficiency was achieved by multiplying $I(x,0)$ by $(L^2+x^2)^{3/2}$.

The Am-241 source used was an electro-deposited source with an active diameter of 2 mm and with a cover of 1.8 mg/cm^2 Ti. On October 15 1998, the source activity was 10 mCi and the alpha particles have approximately 5.4 MeV. This source was desired for the spatial efficiency test because the uniform emission was of atomic particles; this was compatible with the atomic particle detection purpose of the device. The raw spatial response pattern of the detector is evident in fig. 4.6.

Once the laser ionization probability condition and the detector spatial efficiency were known, the sputtering image data processing could occur. Following is an overview of the processing steps as applied to data from the 5 eV Ga program setting. It is important to recall that the program energy setting defined the sputtering energy component along the detector axis direction and normal to the MCP surface.

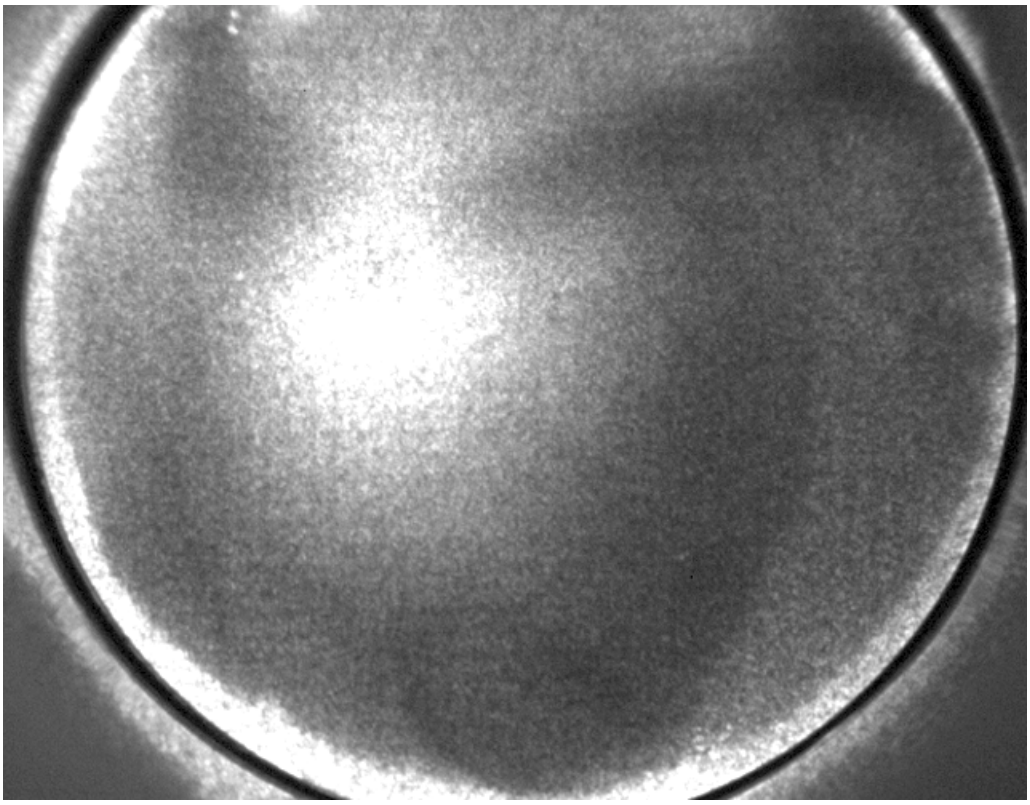

FIGURE 4.6. CCD image taken during spatial efficiency testing for the MCP and Phosphor screen. An Am-241 source placed 77.9 mm from the MCP face produced this signal. For this image, the histogram was modified for improved viewing of the detector response pattern.

Figure 4.7 depicts one of the images of acquired intensities at the 5 eV Ga setting. Three individual images accounting for 6,000 apparatus cycles each were captured for every setting. It was important not to use the Pegasus software averaging routines during initial data acquisition. This allowed visual assurance against stray-light background effects within each image. Approximately five percent of acquired images were afflicted with these effects; they were not incorporated as meaningful data.

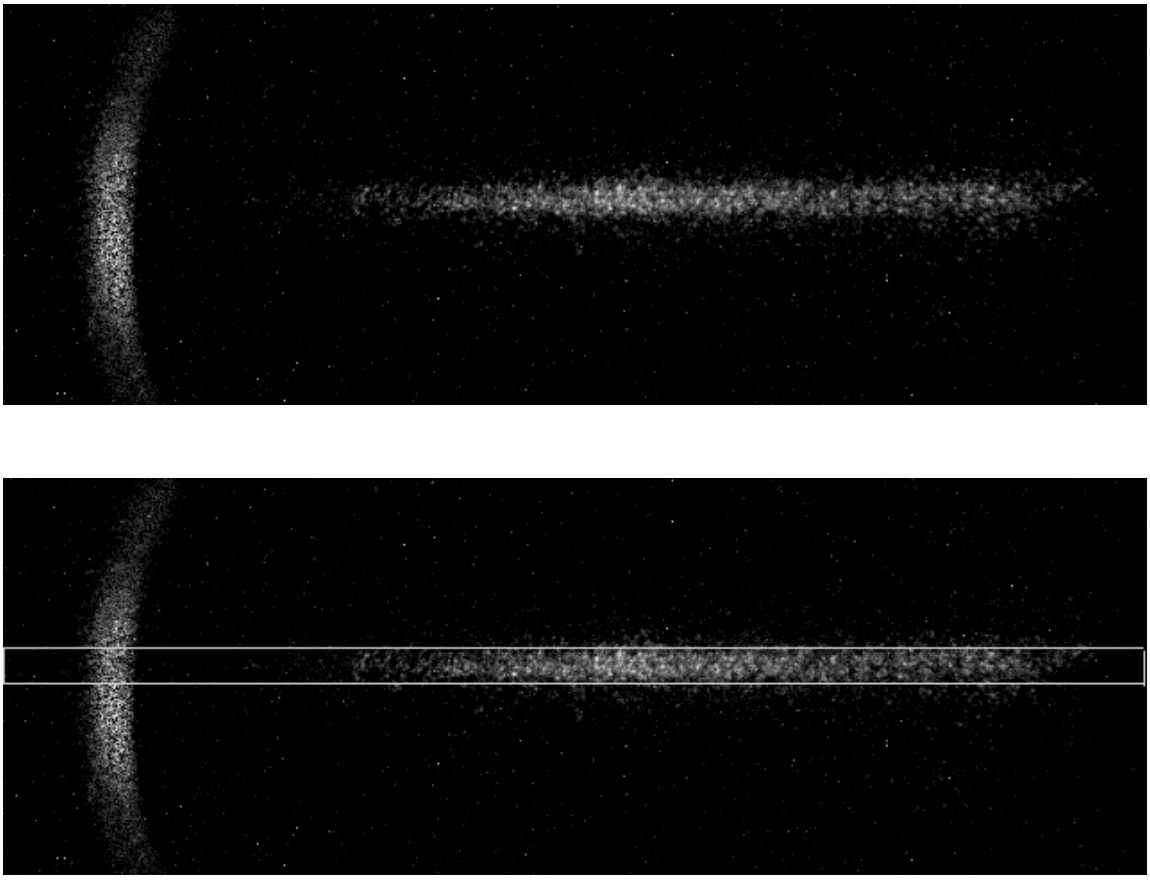

FIGURE 4.7. Two versions of an image of SIRIS signal. Intensity integration was during 6,000 cycles of sputtered Ga at the 5 eV setting. The lower version includes the dynamic data exchange region of interest. The thickness of the region was 20 pixels and the entire image width was selected in order to maintain a pixel-to-detector position correspondence. Laser-induced stray-light background effects are responsible for the intensity arc on the left side.

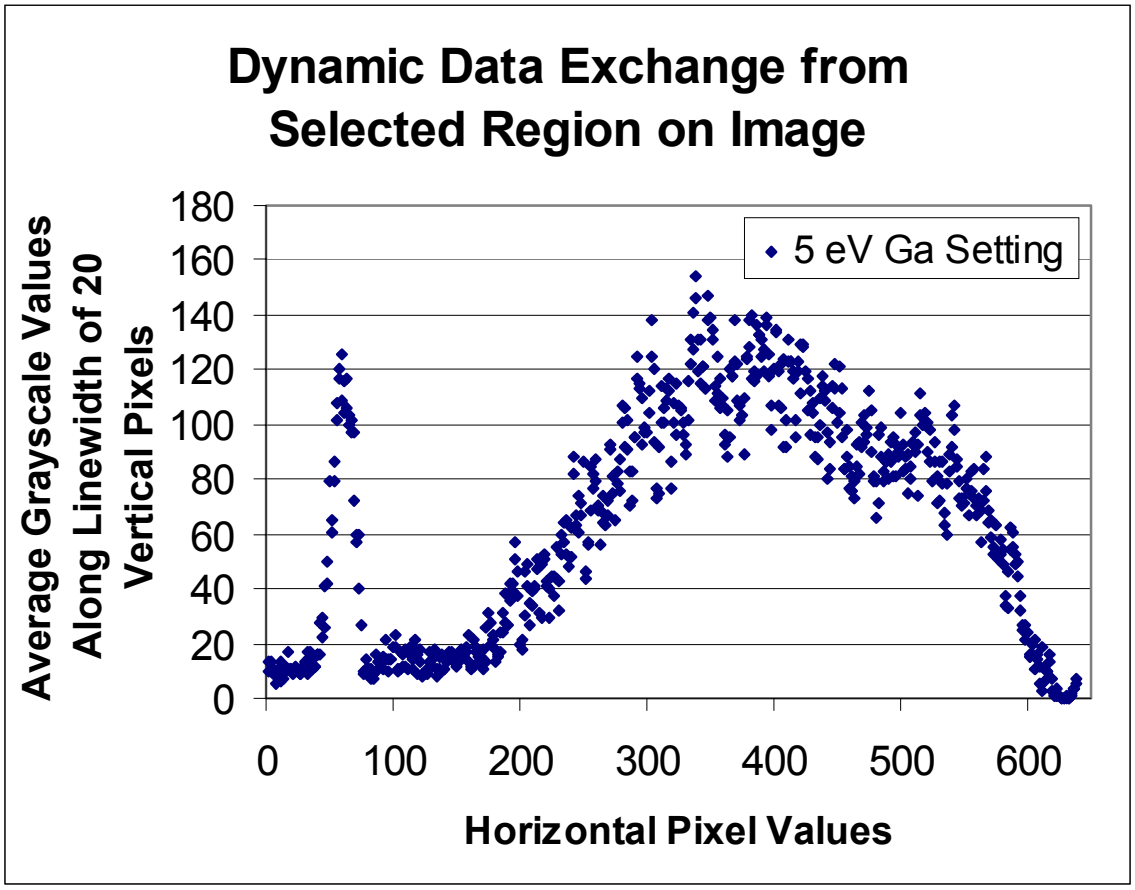

FIGURE 4.8. Plot of image gray scale intensity for the image in fig. 4.7. These values were obtained directly from the dynamic data exchange routine on Global Lab Image software. Again, the intensity spike on the left was due to the laser; it was beyond the sputtering angular emission region of collection and was ignored. The horizontal center of the detector was measured at pixel 302.

Following the dynamic data exchange routine in Global Lab Image, fig. 4.8 depicts the resulting gray-scale values across the region of interest. Figure 4.9 exhibits average signal intensity from three individual images. Such an average accounted for 18,000 apparatus cycles. All data were acquired and compiled in this fashion.

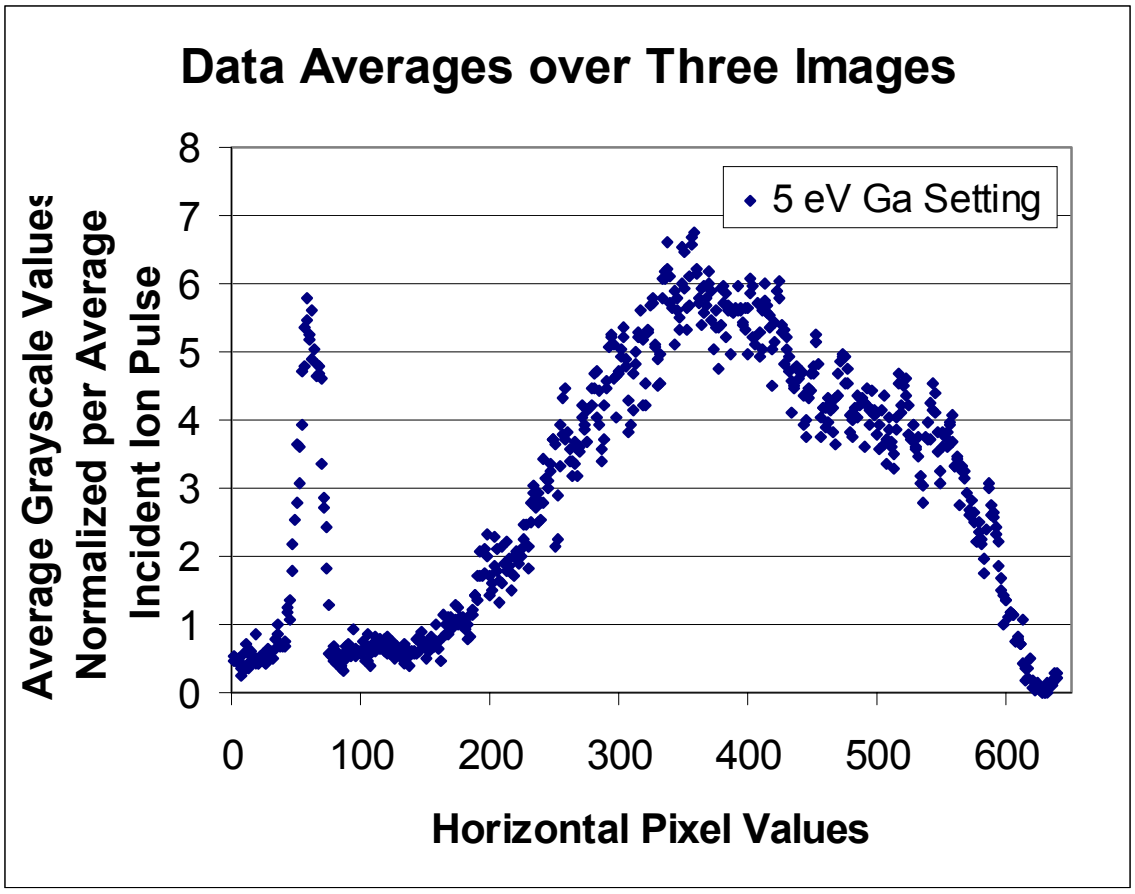

FIGURE 4.9. SIRIS intensity averages of those in fig. 4.8 with two additional representations of identical experimental parameters. Improved statistics demonstrated that the signal intensity profile approached a smooth curve.

Actual spatial efficiency in the detector is plotted in fig. 4.10. These data originated from a region in the image shown in fig 4.6. that corresponded to the SIRIS signal intensity region of interest. Unprocessed and geometrically processed data are both shown. It is obvious that the spatial efficiency is erratic. Also, it was unknown if these variations were due to the MCP, to the phosphor screen, or to both. Still, the spatial efficiency correction was an important step to include. And, it is recommended that future experimental work include a fresh efficiency measurement in case changes occur.

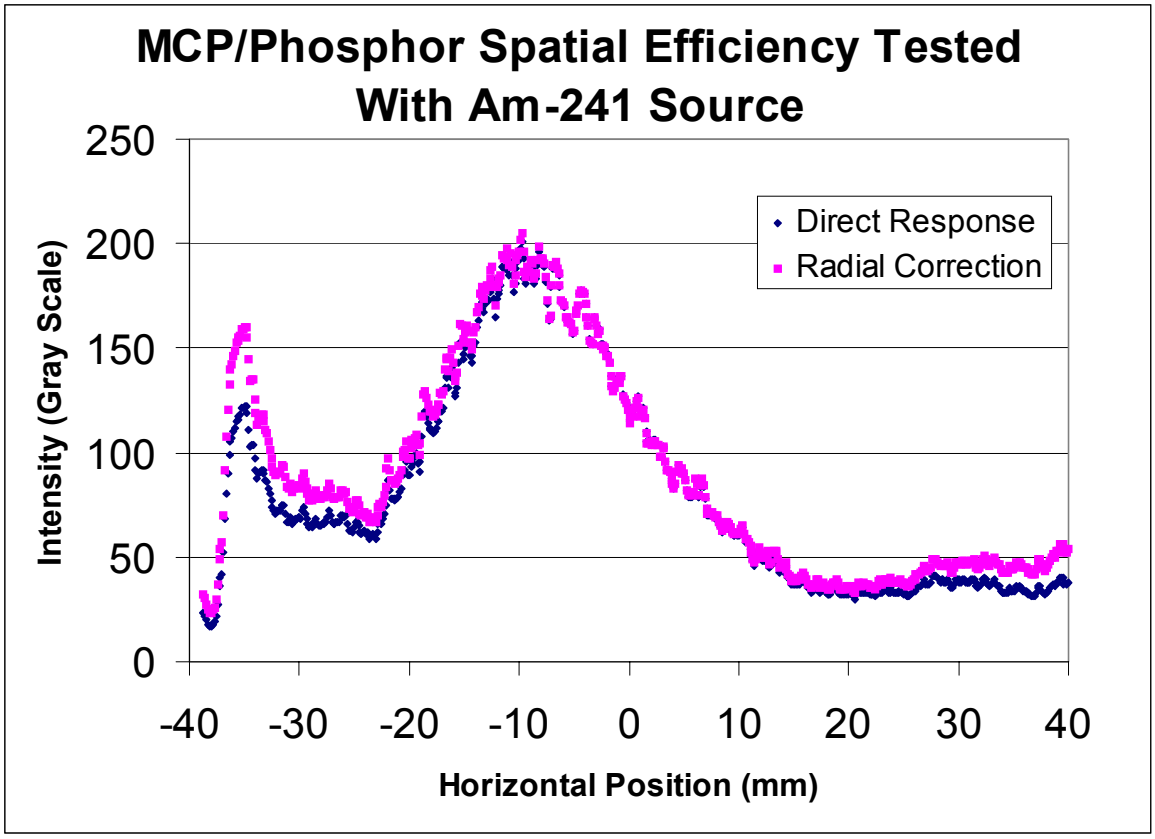

FIGURE 4.10. Horizontal spatial efficiency of the position-sensitive detector. An Americium 241 alpha particle source positioned at the entrance to the detector provided a known, point source of spherical flux. The plot includes the direct intensity response over the SIRIS signal region of interest and the true spatial efficiency following a geometrical correction for a plane intersection with a spherical front. The horizontal axis conversion to the detector dimensions with respect to its horizontal center were made with the conversion, 0.12818 mm/pixel.

Following spatial efficiency correction, the modified image intensities for the 5 eV Ga setting are shown in fig. 4.11. These data were fit with a sixth order polynomial function. The sixth-order fit was used to more accurately view the deconvoluted data later in three-dimensional plot form. Figure 4.12 depicts the detector position to ejection angle tranformation ranges used for Ga in this experiment.

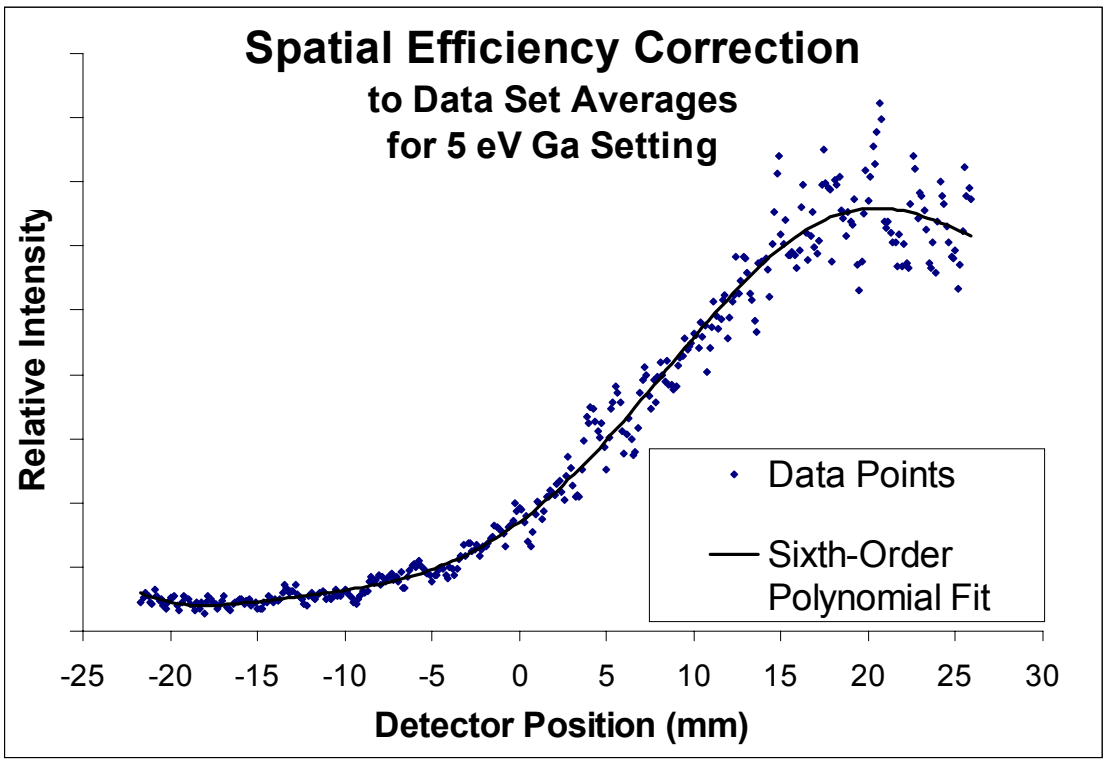

FIGURE 4.11. Detector spatial efficiency correction to SIRIS data. The correction provided intensity normalization to each image. The detector position axis range was cropped to correspond with the angular emission region of interest, 0-85 degrees from sample normal. Data were fit with a sixth-order polynomial.

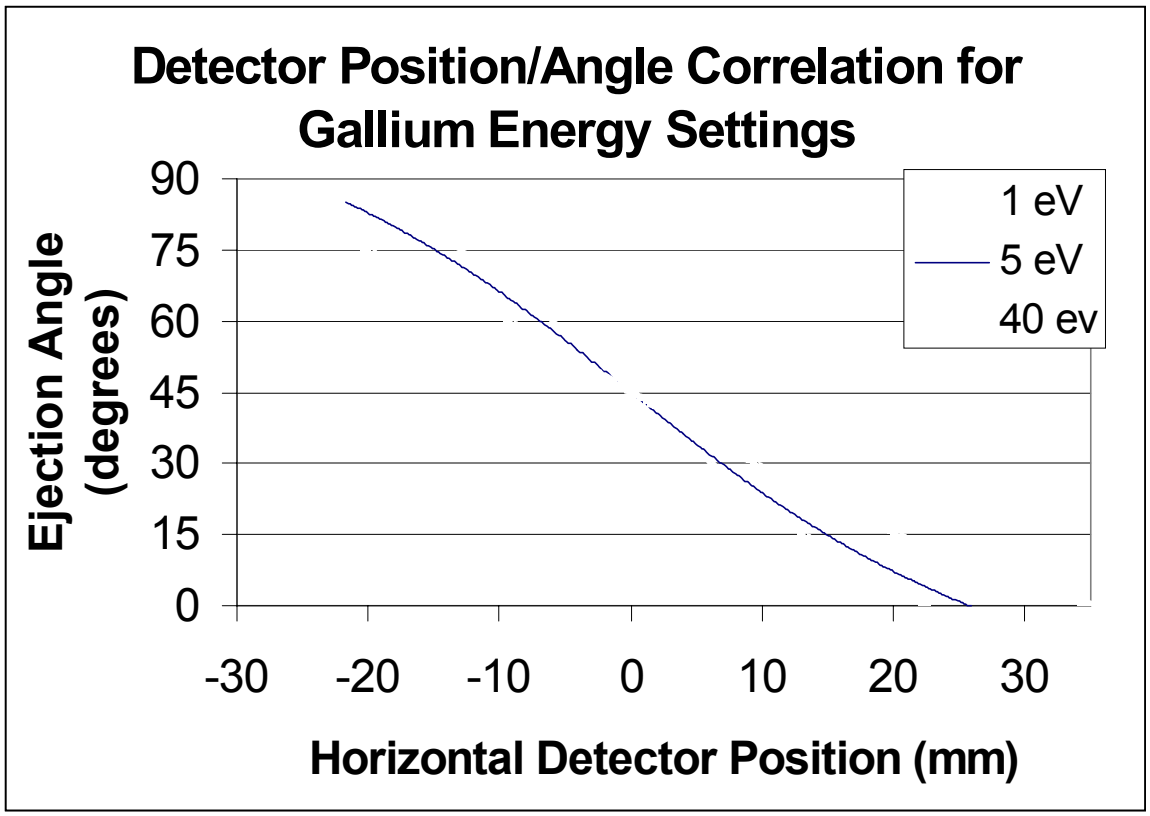

FIGURE 4.12. Graphical representation of the conversions used for signal location on the position-sensitive detector to the sputtering ejection angle. Conversions were dependent on the setting corresponding to unique kinetic energy components along the direction of the detector central axis. The energy setting range used for SIRIS of Ga was 1eV to 40 eV.

Total kinetic energy for each sampled particle was calculated in a straight forward fashion once the ejection angles were known. Using the fact that energy components in a cartesian coordinate system sum together to produce total energy, the transformation to total kinetic energy, $K.E._{Total}$ was given by the expression

$$K.E._{Total} = K.E._{z}(1+\tan\theta), \tag{4.7}$$

where $K.E._{z}$ was the particle kinetic energy component along the central detector axis and q was the sputter ejection angle measured from the detector central axis.

After the sputtering data were converted from impact positions to unique ejection angles and energies, the image intensity was converted to a differential sputtering yield with respect to energy and angle. Refer to the diagram in fig. 4.13 for identification of sputtering event variables used in this next transformation. The position z_g marks the location of the mesh grid, where the electric field is established inside the detector; this variable will be used later in the error analysis section of the text.

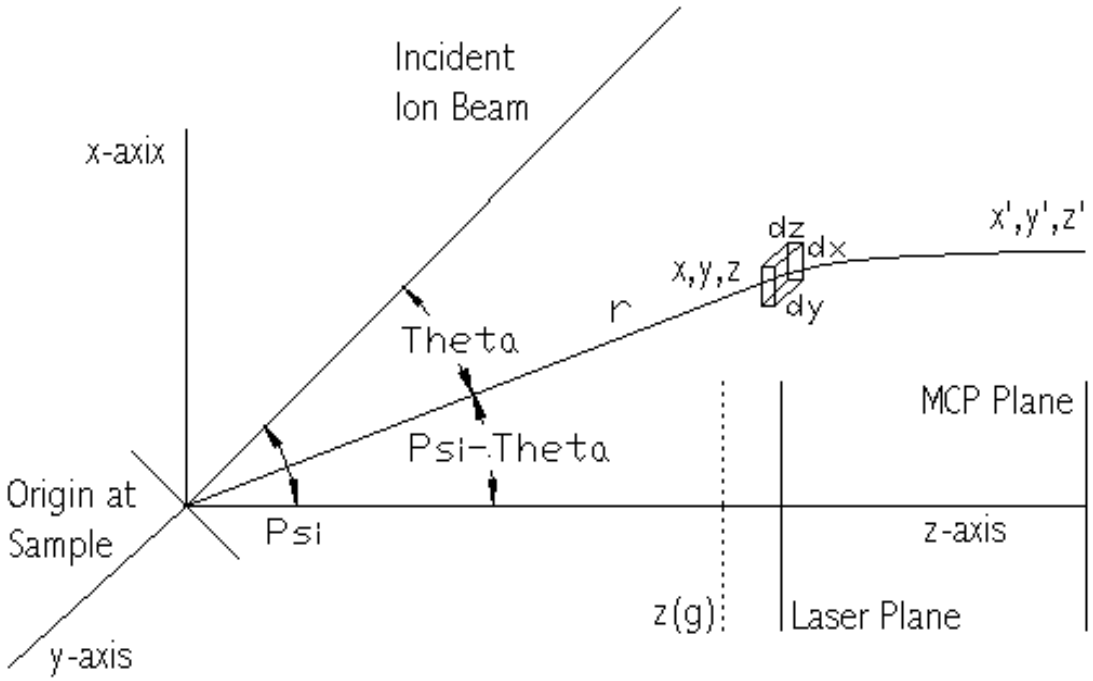

FIGURE 4.13. Diagram of the sputtering event used to derive the differential sputtering yield with respect to energy and angle. The volume element defined by *dx*, *dy*, and *dz* is located within the RIS interaction region.

A projection of the area element defined by *dx* and *dy* onto a solid angle, *d*W, subtending from the source is given by the expression

$$d\Omega = \frac{dx\cos(\psi-\theta)dy}{r^2} = \frac{\cos^3(\psi-\theta)}{z^2}dxdy\,, \tag{4.8}$$

using

$$r = \frac{z}{\cos(\psi - \theta)}, \tag{4.9}$$

where (y-q) is the sputtering ejection angle with respect to the detector central axis (the z-axis), *r* is the flight distance for a sputtered neutral particle, and *z* is the perpendicular distance from the projectile origin to the laser plane. The linear elements at the laser plane, *dx* and *dy*, scale linearly with time from the corresponding linear elements mapped onto the MCP plane, *dx'* and *dy'*. The scale is simply the ratio between the neutral flight time to the laser plane, *t*, and the total time for the particle to travel from the sample to the MCP, *t'*. With this in mind, the solid angle expression in terms of the differential position elements at the plane of the MCP, the data collection area, is transformed to

$$d\Omega = \left(\frac{t}{t'}\right)^2 \frac{\cos^3(\psi - \theta)}{z^2} dx'dy'. \tag{4.10}$$

Total initial kinetic energy, *E*, of the particle of mass, *m*, is expressed as

$$E = \frac{m}{2}\left(\frac{r}{t}\right)^2 = \frac{m}{2}\left(\frac{z}{t\cos(\psi - \theta)}\right)^2. \tag{4.11}$$

The energy differential term is

$$dE = \frac{mz}{t^2\cos^2(\psi - \theta)} dz. \tag{4.12}$$

The measured intensities, *M*, are expressed as differential yields with the expression

$$M = \frac{dY}{dEd\Omega}\Delta E\Delta\Omega. \tag{4.13}$$

Incorporating the earlier differential expressions, *dE* and *d*W, and ignoring constant components, the differential sputtering yield simplifies to the proportionality

$$\frac{dY}{dEd\Omega} \propto \frac{Mt'^2}{\cos(\psi-\theta)\Delta z}, \tag{4.14}$$

where *t'* is solved from basic projectile equations and Δz is the width of the laser beam.

The differential sputtering yield for the 5 eV Ga setting is plotted in fig 4.14

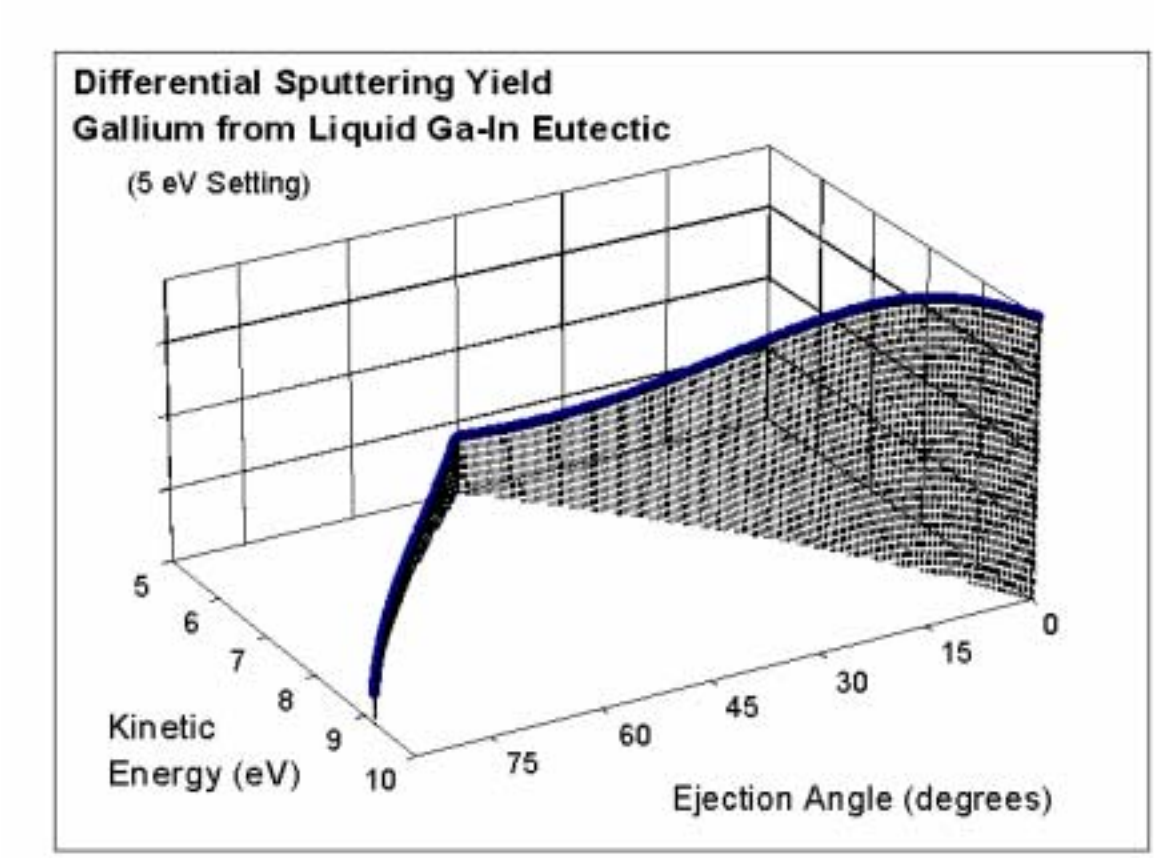

FIGURE 4.14. The differential sputtering yield with respect to energy and angle. This representation followed several transformation steps applied to the CCD image intensities gathered at the 5 eV Ga setting; it exhibits the image position deconvolution into angle and energy.

The differential sputtering yield, $\frac{dY}{dEd\Omega}$, was expressed in three-dimensional surface plots as a function of energy and angle in fig. 4.15-4.18. Two-dimensional contour plots of the same data are shown in fig. 4.19 and 4.20.

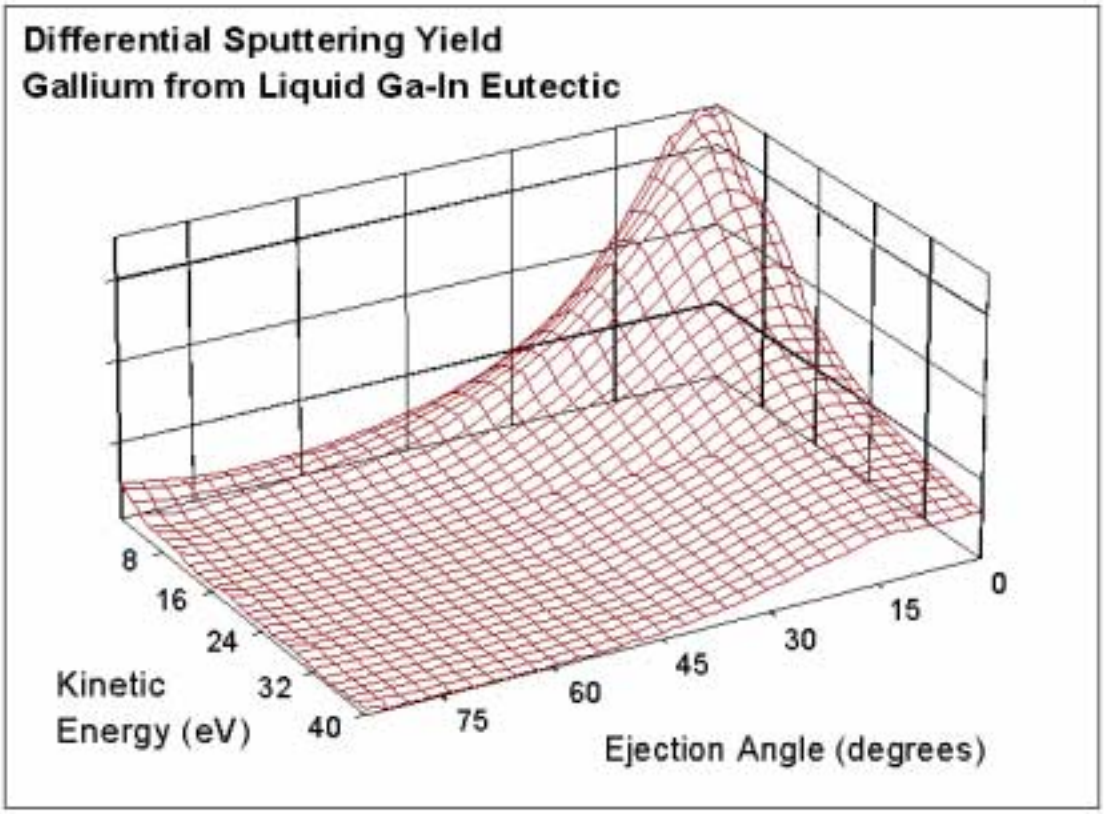

FIGURE 4.15. Grid plot of the differential sputtering yield with respect to energy and angle for Ga sputtered from liquid Ga-In eutectic alloy. The grid surface helps to view the energy peak in the distribution.

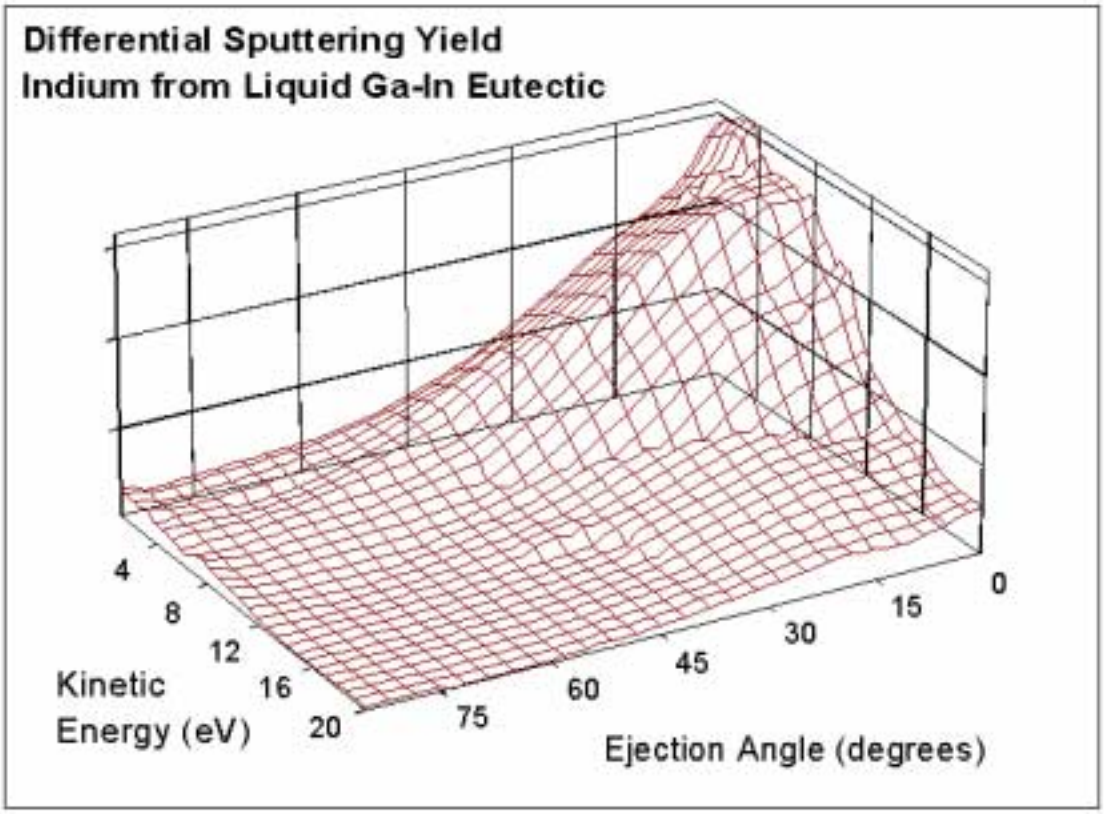

FIGURE 4.16. The differential sputtering yield with respect to energy and angle for In sputtered from liquid Ga-In eutectic alloy. Compared to the plot in fig. 4.15, the differential yield for In is broader in angle and narrower in energy. Note that the energy axis covers a smaller range than in fig. 4.15.

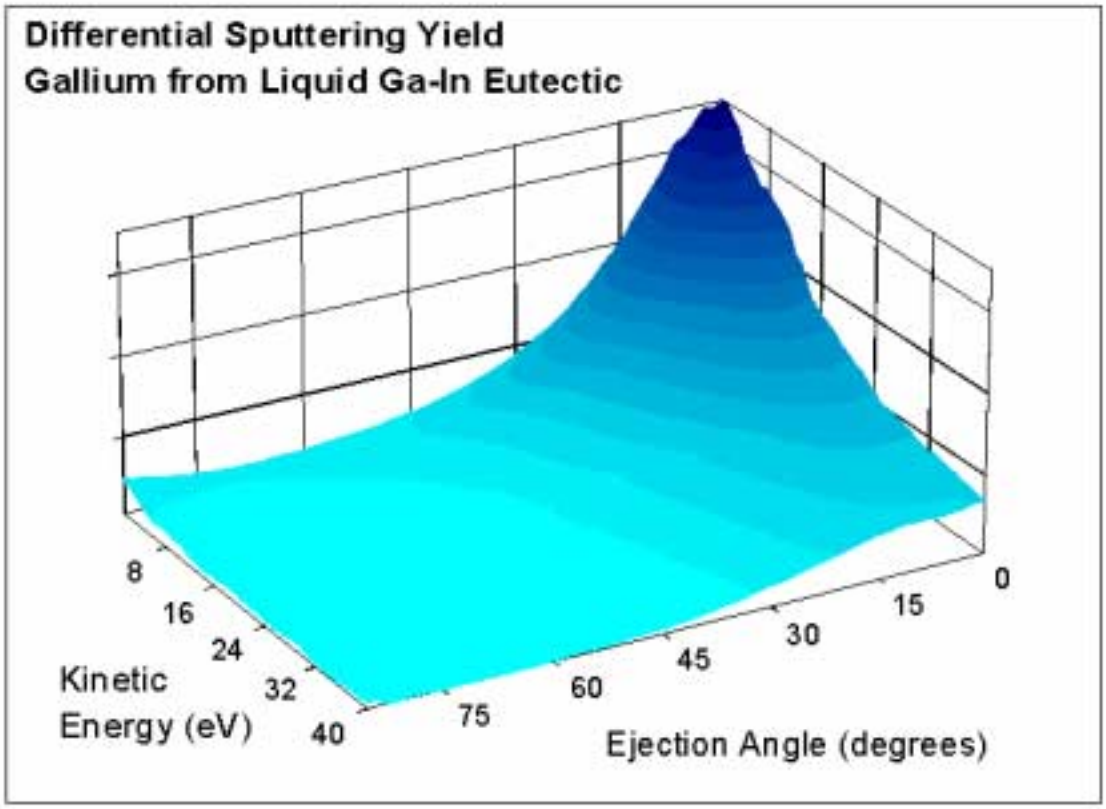

FIGURE 4.17. The differential sputtering yield with respect to energy and angle for Ga sputtered from liquid Ga-In eutectic alloy. This type of three-dimensional contour plot allows a perspective into the gradient of the differential sputtering yield.

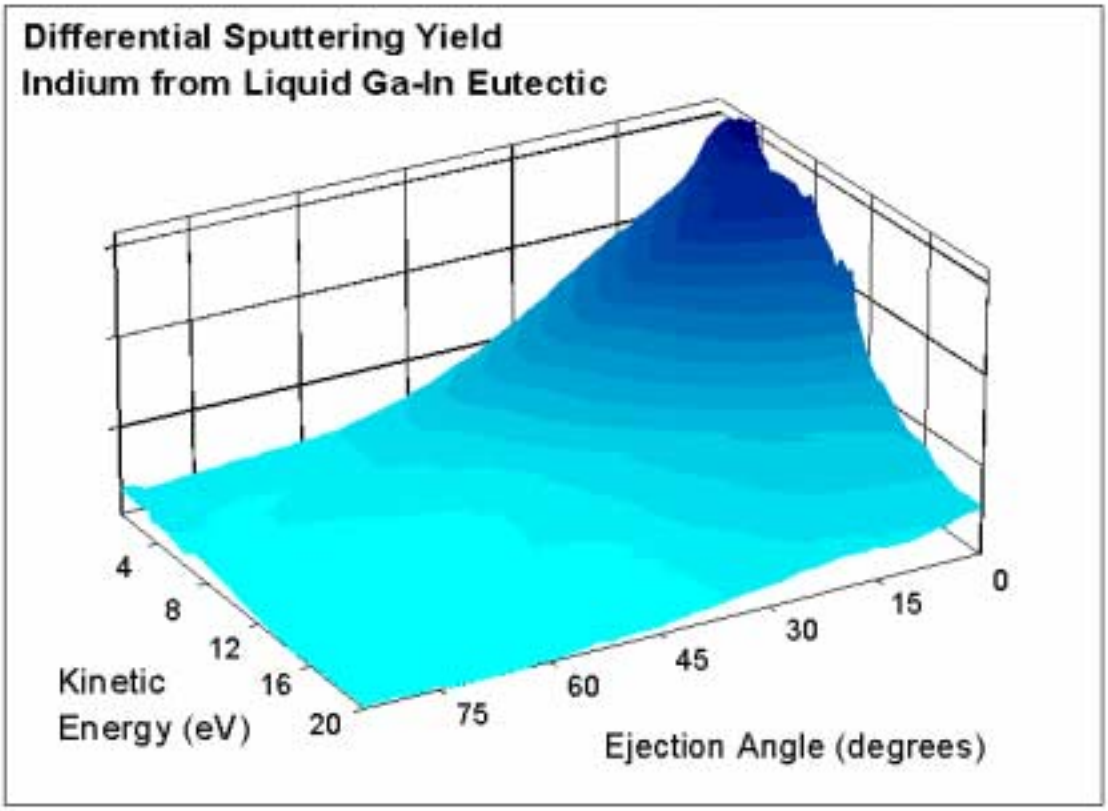

FIGURE 4.18. The differential sputtering yield with respect to energy and angle for In sputtered from liquid Ga-In eutectic alloy.

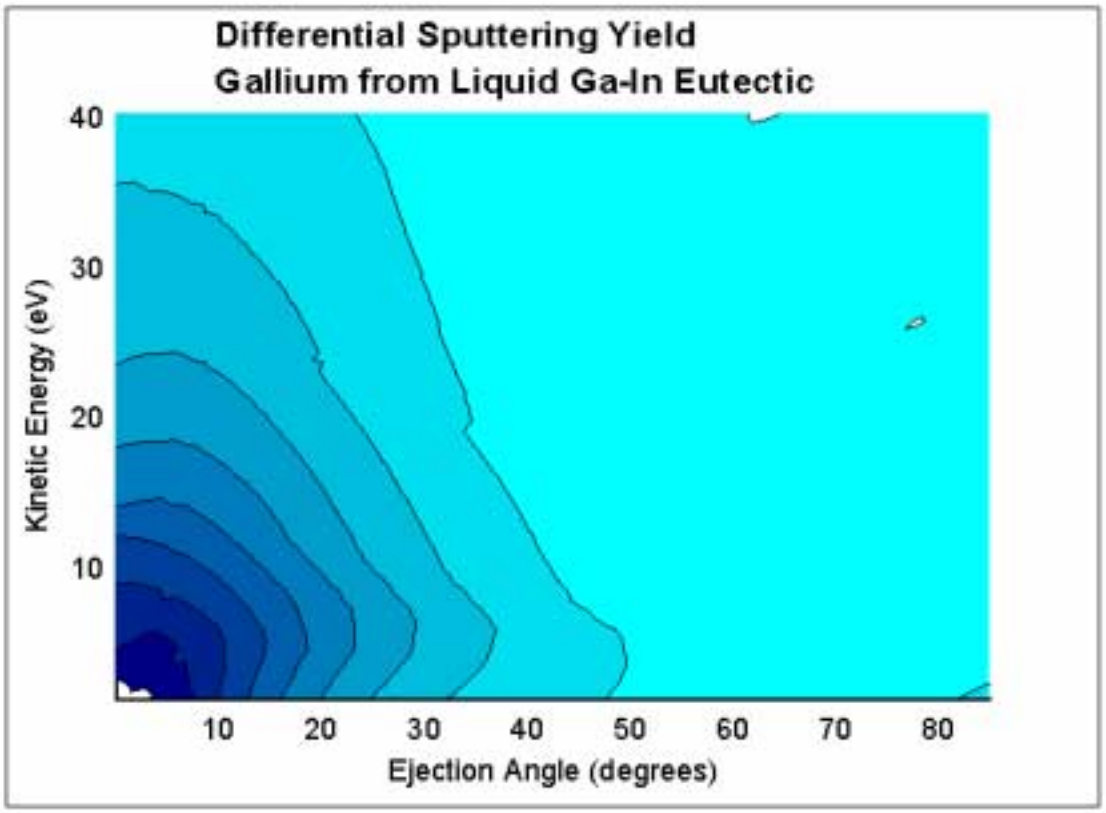

FIGURE 4.19. Contour plot of the differential sputtering yield with respect to energy and angle for Ga sputtered from liquid Ga-In eutectic alloy.

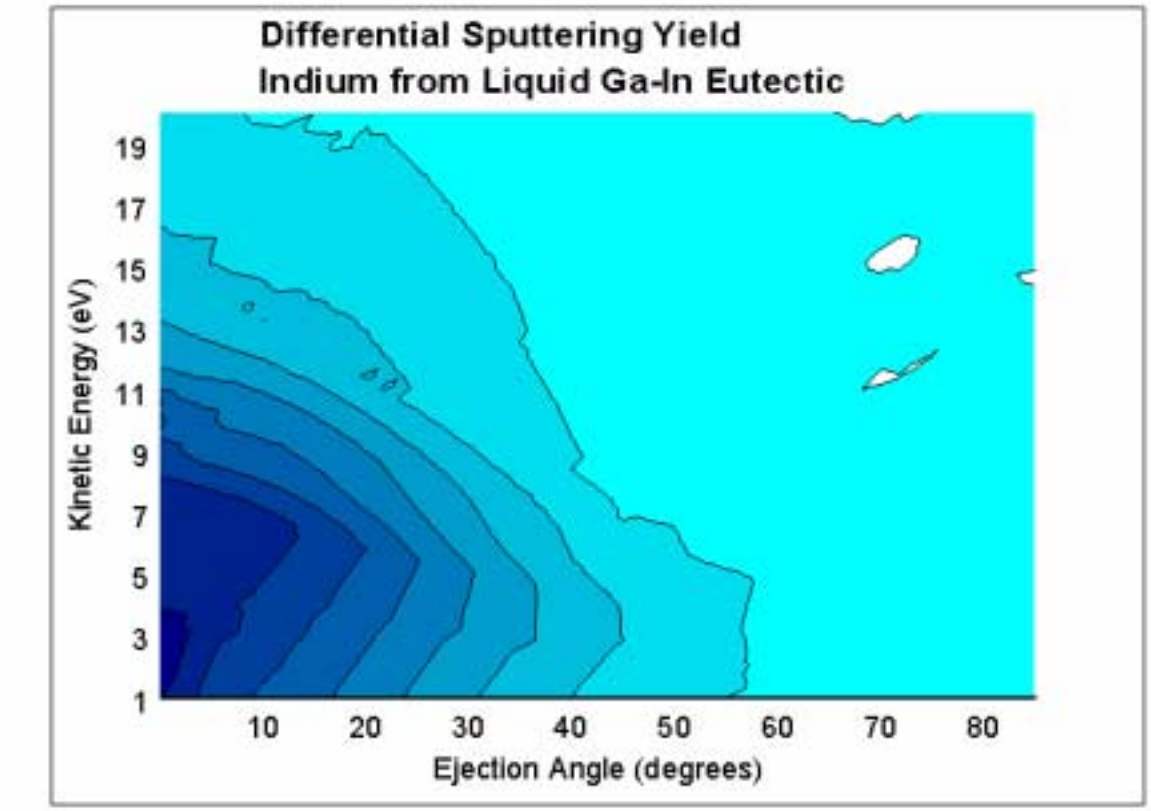

FIGURE 4.20. Contour plot of the differential sputtering yield with respect to energy and angle for In sputtered from liquid Ga-In eutectic alloy.

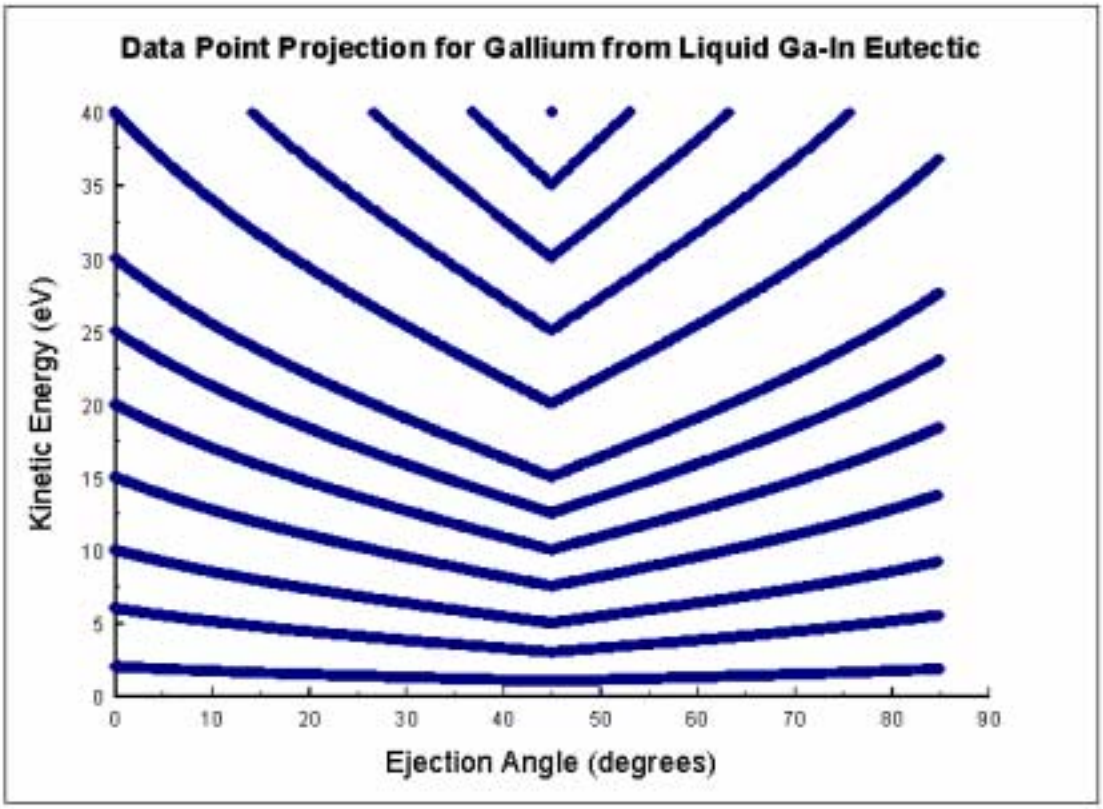

FIGURE 4.21. The actual values of energy and angle sampled for the Ga sputtering data.

In fig. 4.21 and 4.22, the sputtering data points for Ga and In are projected onto the angle and energy plane. Each curve on these plots was derived from image intensity data corresponding to a single setting on the SIRIS apparatus. At the maximum energy extents, the data curves were cropped to match the boundaries of the data presentation. Hence, only portions of those data curves were included in the data analysis. The reason for including these views of the data points was to provide a reminder that the data coverage was limited. Gaps in the energy spectra existed and the three-dimensional plotting routines tended to fill in the missing data. With this in mind, prudence is urged in drawing conclusions from the data plots, especially at the minimum energy extent.

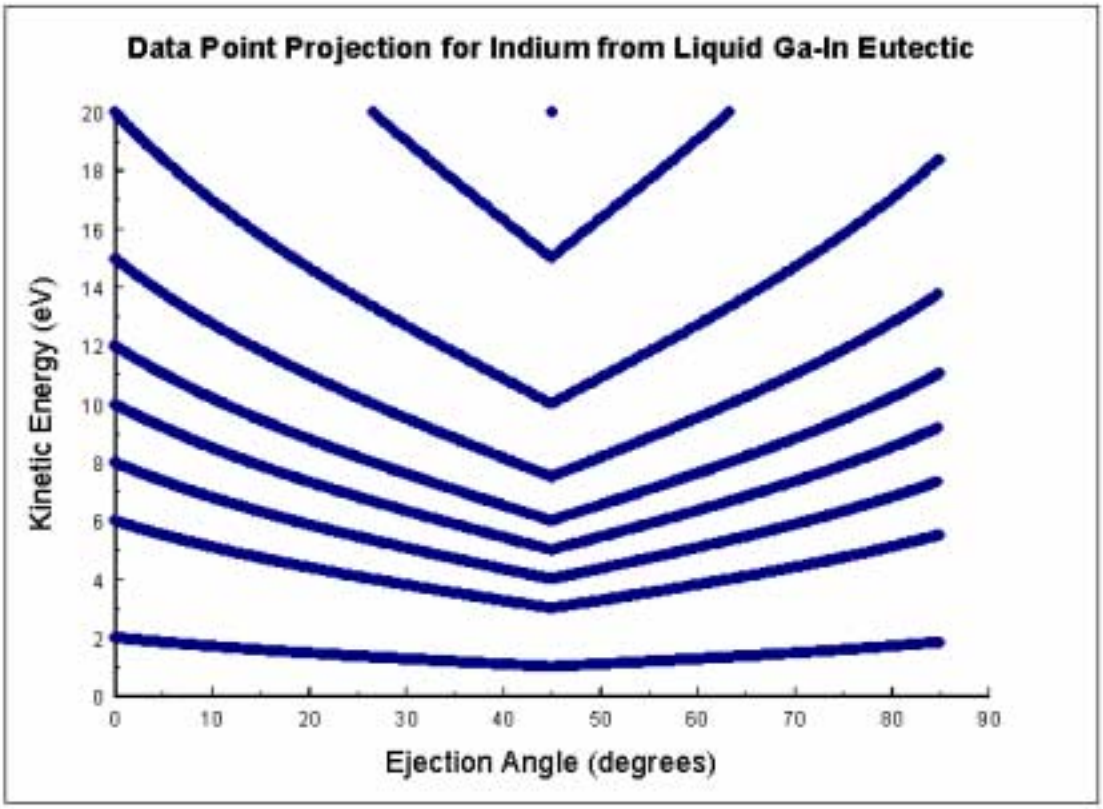

FIGURE 4.22. The actual values of energy and angle sampled for the In sputtering data.

Final presentation of the results for the differential sputtering yields for Ga and In from liquid Ga-In eutectic involved integrating over the energy and angle variables, respectively. Following integration over the energy spectra at 5-degree angular increments, the angular distribution for the sputtered particles was deduced; this distribution is plotted in fig. 4.23. The maximum points in the angular distribution plots were normalized with respect to each other and arbitrary yield units were used. From these distributions, the results have qualitative agreement to the previous studies of sputtering behavior from the liquid Ga-In eutectic. However, the distributions were not fit well by the $\sin(q)$-weighted $\cos^n(q)$ model used by Hubbard et al. (6). The limited data

set may explain the poor fit. Data for energies less than those obtained from a minimum 1 eV setting used with the spectrometer could have played an important role in the angular distribution discrepancy.

A second potential cause for the poor comparison could have been an uncertain sample surface condition. The delicate sample introduction procedure was describe earlier; however, there was no method employed during the experiment to monitor a possible surface oxide layer. On the other hand, after the data presented here were gathered, the sample was deliberately exposed to atmospheric conditions to expedite the formation of a surface Ga oxide layer. During subsequent SIRIS experimentation, In was nearly undetectable from the oxidized sample; this trial merely suggests that the sample surface was not oxidized during the principle measurements, but doesn't prove that the surface was atomically clean.

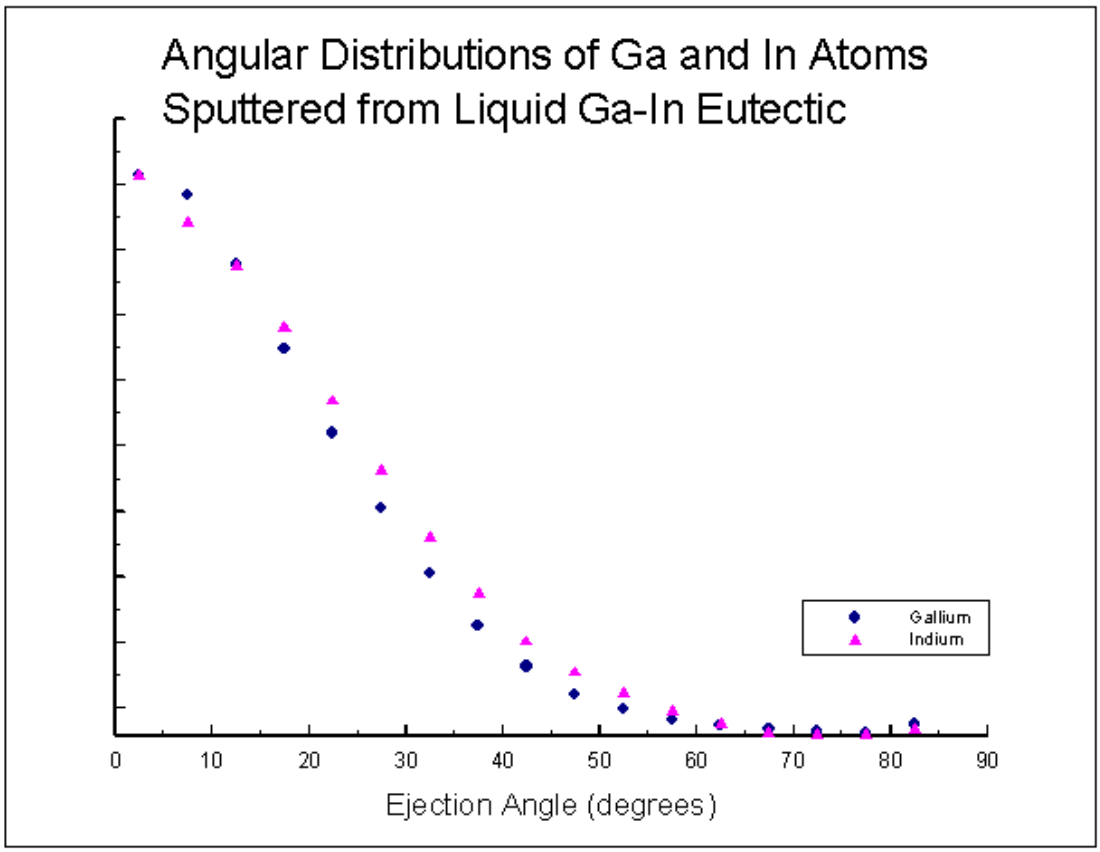

FIGURE 4.23. The angular distributions of sputtered Ga and In atoms from liquid Ga-In eutectic.

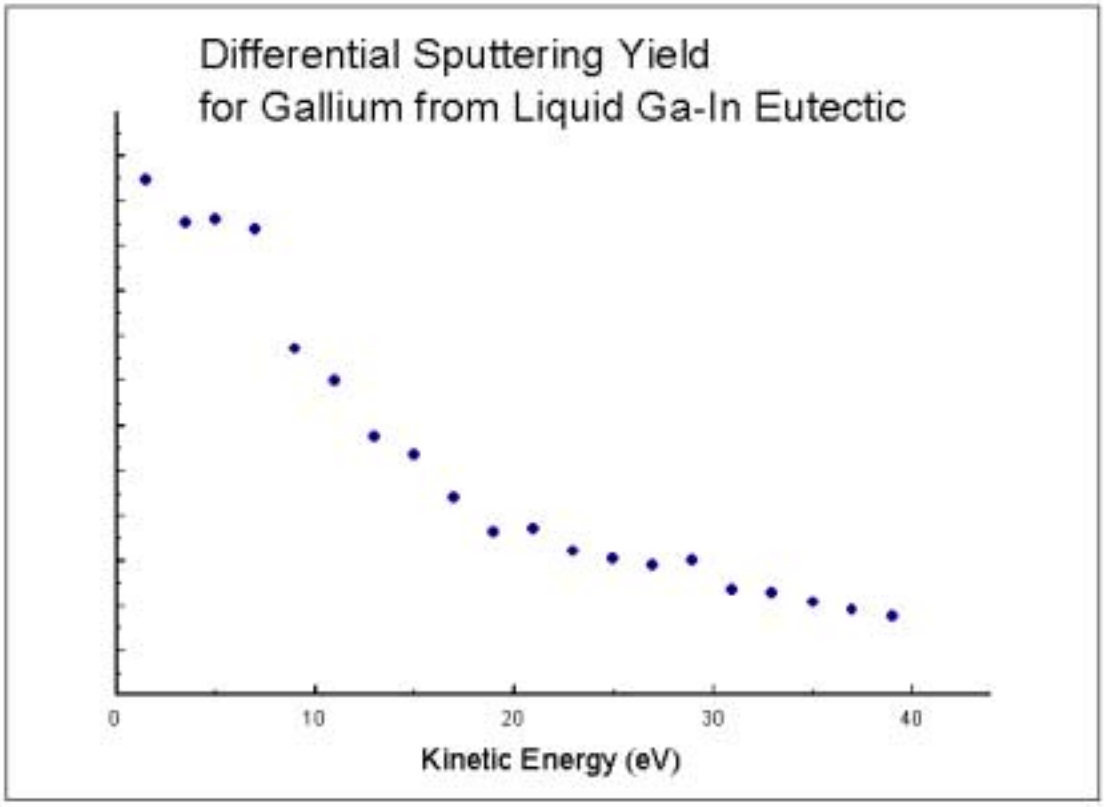

FIGURE 4.24. The energy distribution of sputtered Ga atoms from liquid Ga-In eutectic alloy.

The energy distributions for sputtered Ga and In atoms from liquid Ga-In eutectic alloy are shown in fig. 4.24 and 4.25, respectively. These plots were arrived at after the differential sputtering yields were integrated over angles at energy increments of 1 eV for In and 2 eV for Ga. Slight increment adjustments were made for the lowest energy values because of the data set limitations. Distortions to the distributions due to these slight adjustments were not expected. The data increments by energy were simple to integrate using the $\cos^n(q)$ fit discussed earlier. Although the fit was not extremely accurate, the resulting points along the energy distribution compared well with a similar data processing routine that employed a more accurate angular fit.

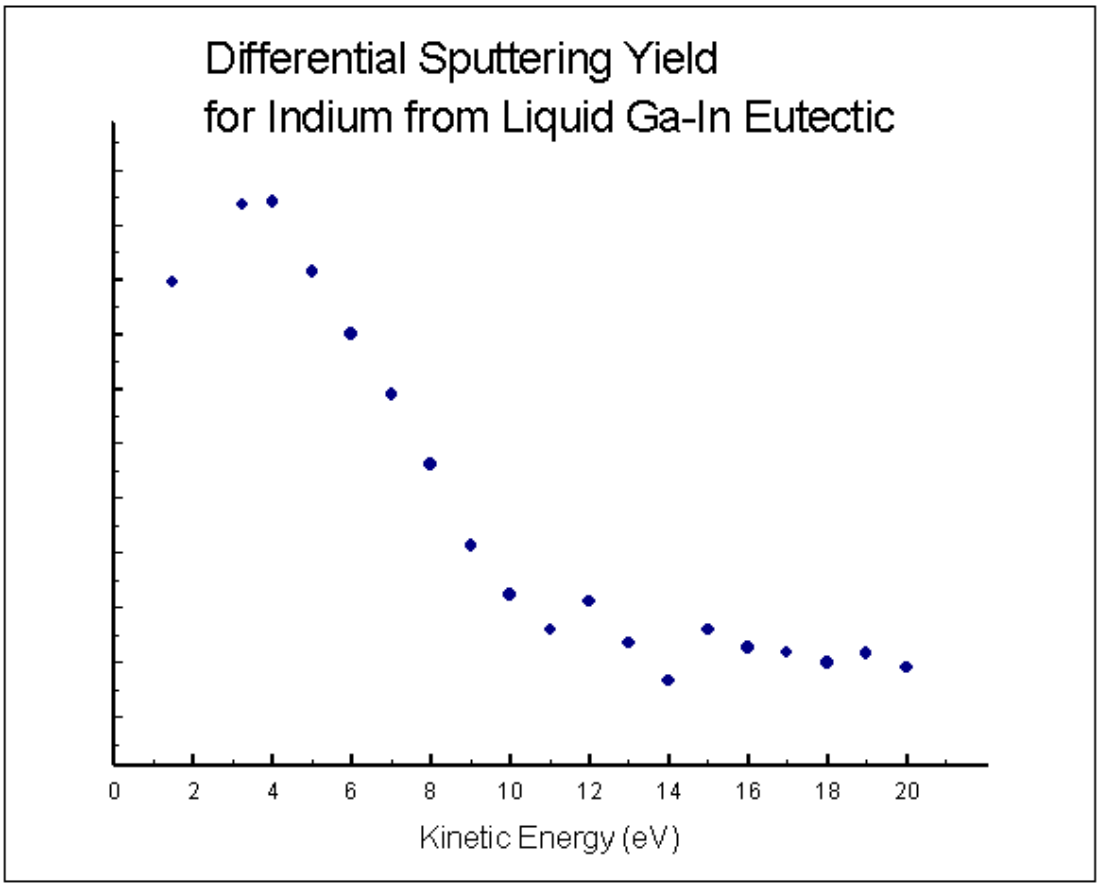

FIGURE 4.25. The energy distribution of sputtered In atoms from liquid Ga-In eutectic alloy

At this point, a general remark is that the differential sputtering yields for Ga and for In from the liquid Ga-In eutectic exhibit the trends that were expected. For In, the sputtering pattern is characteristic of sputtering from the top layer of a sample. The yields are broader in angle and concentrated at lower energies. For Ga, on the other hand, the differential sputtering yields are significantly sharper in angle and they include sputtered particles with significantly higher energies. For the energy distributions, there is a

qualitative agreement with the molecular dynamics simulation (14). Discrepancies could still be caused by an incomplete data set gathered in this SIRIS experiment.

Error Analysis

To arrive at the uncertainty in the differential sputtering yields, each experimental variable in the yield expression must be considered. This yield expression, with all terms included, is

$$\frac{dY}{dEd\Omega} = \frac{M}{\cos(\psi-\theta)} \cdot \frac{zt'^2}{m} \cdot \frac{1}{\Delta x' \Delta y' \Delta z}. \tag{4.15}$$

The variables were defined earlier in this chapter when the differential sputtering yield was derived; and, the diagram in fig. 4.13 is a helpful reminder. The incremental length elements are treated as constants. The uncertainty in the expression for the differential sputtering yield is

$$\sigma = \sqrt{\left(\frac{\partial Y}{\partial M}\right)^2 \sigma_M^2 + \left(\frac{\partial Y}{\partial(\psi-\theta)}\right)^2 \sigma_{\psi-\theta}^2 + \left(\frac{\partial Y}{\partial z}\right)^2 \sigma_z^2 + \left(\frac{\partial Y}{\partial t'}\right)^2 \sigma_{t'}^2}, \tag{4.16}$$

where Y represents the differential sputtering yield. The partial derivatives of Y with respect to each of the uncertainty variables are listed below.

$$\frac{\partial Y}{\partial M} = \frac{1}{\cos(\psi-\theta)} \cdot \frac{zt'^2}{m} \cdot \frac{1}{\Delta x' \Delta y' \Delta z} \tag{4.17}$$

$$\frac{\partial Y}{\partial z} = \frac{M}{\cos(\psi-\theta)} \cdot \frac{t'^2}{m} \cdot \frac{1}{\Delta x' \Delta y' \Delta z} \tag{4.18}$$

$$\frac{\partial Y}{\partial t'} = \frac{M}{\cos(\psi-\theta)} \cdot \frac{2zt'}{m} \cdot \frac{1}{\Delta x' \Delta y' \Delta z} \tag{4.19}$$

$$\frac{\partial Y}{\partial(\psi-\theta)} = \frac{M\sin(\psi-\theta)}{\cos^2(\psi-\theta)} \cdot \frac{zt'^2}{m} \cdot \frac{1}{\Delta x' \Delta y' \Delta z} \tag{4.20}$$

The uncertainty, s_M, was obtained by considering the number of standard deviations needed to envelop typical signal intensity values in fig. 4.7. A strong estimate for the envelope is ±20% from the signal mean. Statistical theory states that three standard deviations measured from the arithmetic mean include 99.73% of all values (39). With this technique, the uncertainty, s_M, was chosen as an over-estimate to one standard deviation, 7% of the arithmetic mean.

The uncertainty s_z relates directly to the width of the resonance ionization laser beam. Again, the width of the resonance ionization region was defined by the width of the second harmonic components. Approximating this region with a rectangle, the width of the second harmonic component of the laser beam was treated as 0.5 mm. Hence, the uncertainty, at half the width value, was deemed 0.25 mm.

The total time for a sputtered particle to translate from the sample to the MCP, *t*', also contributed to the differential sputtering yield. As mentioned earlier in the text, this time was the solution to an equation for classical projectile motion,

$$t' = t + \frac{mz(z'-z)}{Ut}\left(\sqrt{1+\frac{2Ut^2}{mz^2}}-1\right), \tag{4.21}$$

where U is the potential energy of the ion at the point of photoionization. With z_g as the position of the first grid in the detector, at one end of the electric field region,

$$U = \frac{qV(z'-z)}{z'-z_g}. \tag{4.22}$$

The variables that contributed uncertainty to *t*' were *t* and *z*. Hence,

$$\sigma_{t'} = \sqrt{\left(\frac{\partial t'}{\partial t}\right)^2 \sigma_t^2 + \left(\frac{\partial t'}{\partial z}\right)^2 \sigma_z^2}\,, \tag{4.23}$$

$$\frac{\partial t'}{\partial t} = 1 - \frac{mz(z'-z)}{Ut^2}\left(\sqrt{1+\frac{2Ut^2}{mz^2}} - 1\right) + \frac{2(z'-z)}{z}\cdot\frac{1}{2}\left(1+\frac{2Ut^2}{mz^2}\right)^{-1/2}, \tag{4.24}$$

$$\frac{\partial t'}{\partial z} = \frac{m(z'-z)}{Ut}\left(\sqrt{1+\frac{2Ut^2}{mz^2}} - 1\right) + \frac{t}{z}\left(\frac{1}{z}+1\right)\left(1+\frac{2Ut^2}{mz^2}\right)^{-1/2}. \tag{4.25}$$

For the uncertainty in time, s_t, the duration of the primary ion pulse that initiated the sputtering process was 200 ns. It was difficult to ascertain the exact temporal shape of this ion pulse when it arrived on the sample. However, the voltage pulse used to produce the ion pulse was rectangular. So, this temporal uncertainty was estimated to be half the ideal ion pulse duration, or 100 ns. The uncertainty, s_z, retained its value discussed above at 0.25 mm.

The angular uncertainty, $s_{(y\text{-}q)}$, also contained imbedded terms. To simplify this expression, the angular uncertainty treatment was limited to the horizontal plane. As well, the angle y remained at 45 degrees during the experiment. With these simplifications and after an applied coordinate rotation to the angular expression, the polar ejection angle with respect to the target normal, q', is

$$\theta' = \arccos\left[\frac{1}{2}\sqrt{\frac{m}{E}}\left(\frac{x'}{t'}+\frac{z}{t}\right)\right]. \tag{4.26}$$

The uncertainty for this angle is

$$\sigma_{\theta'} = \sqrt{\left(\frac{\partial\theta'}{\partial E}\right)^2\sigma_E^2 + \left(\frac{\partial\theta'}{\partial x'}\right)^2\sigma_{x'}^2 + \left(\frac{\partial\theta'}{\partial z}\right)^2\sigma_z^2 + \left(\frac{\partial\theta'}{\partial t}\right)^2\sigma_t^2 + \left(\frac{\partial\theta'}{\partial t'}\right)^2\sigma_{t'}^2} \tag{4.27}$$

The partial derivatives are:

$$\frac{\partial\theta'}{\partial E}=\frac{-1}{\sqrt{1-\left[\frac{1}{2}\sqrt{\frac{m}{E}}\left(\frac{x'}{t'}+\frac{z}{t}\right)\right]^2}}\left[\frac{-\sqrt{m}}{4}\left(\frac{x'}{t'}+\frac{z}{t}\right)E^{-3/2}\right], \tag{4.28}$$

$$\frac{\partial\theta'}{\partial x'}=\frac{-1}{\sqrt{1-\left[\frac{1}{2}\sqrt{\frac{m}{E}}\left(\frac{x'}{t'}+\frac{z}{t}\right)\right]^2}}\left(\frac{1}{2t'}\sqrt{\frac{m}{E}}\right), \tag{4.29}$$

$$\frac{\partial\theta'}{\partial z}=\frac{-1}{\sqrt{1-\left[\frac{1}{2}\sqrt{\frac{m}{E}}\left(\frac{x'}{t'}+\frac{z}{t}\right)\right]^2}}\left(\frac{1}{2t}\sqrt{\frac{m}{E}}\right), \tag{4.30}$$

$$\frac{\partial\theta'}{\partial t}=\frac{-1}{\sqrt{1-\left[\frac{1}{2}\sqrt{\frac{m}{E}}\left(\frac{x'}{t'}+\frac{z}{t}\right)\right]^2}}\left(\frac{-z}{2t^2}\sqrt{\frac{m}{E}}\right), \tag{4.31}$$

$$\frac{\partial\theta'}{\partial t'}=\frac{-1}{\sqrt{1-\left[\frac{1}{2}\sqrt{\frac{m}{E}}\left(\frac{x'}{t'}+\frac{z}{t}\right)\right]^2}}\left(\frac{-x'}{2t'^2}\sqrt{\frac{m}{E}}\right). \tag{4.32}$$

Uncertainties within the angular expression have already been treated except for the uncertainty in the energy, s_E, which contains terms for time and position. Energy is expressed as

$$E=\frac{m}{2}\left[\left(\frac{x'}{t'}\right)^2+\left(\frac{z}{t}\right)^2\right]. \tag{4.33}$$

The energy uncertainty term and its associated partial derivatives are:

$$\sigma_E=\sqrt{\left(\frac{\partial E}{\partial x'}\right)^2\sigma_{x'}^2+\left(\frac{\partial E}{\partial z}\right)^2\sigma_z^2+\left(\frac{\partial E}{\partial t}\right)^2\sigma_t^2+\left(\frac{\partial E}{\partial t'}\right)^2\sigma_{t'}^2}\,, \tag{4.34}$$

$$\frac{\partial E}{\partial x'} = \frac{mx'}{t'^2}, \tag{4.35}$$

$$\frac{\partial E}{\partial z} = \frac{mz}{t^2}, \tag{4.36}$$

$$\frac{\partial E}{\partial t} = -\frac{mz^2}{t^3}, \tag{4.37}$$

$$\frac{\partial E}{\partial t'} = -\frac{mx'^2}{t'^3}. \tag{4.38}$$

CHAPTER 5

CONCLUSION

The SIRIS experimental apparatus used in this experimental work beautifully combined low-energy particle accelerator techniques with laser technology. And, the apparatus was successful at measuring the differential sputtering yields for Ga and for In from the liquid Ga-In eutectic alloy. The differential sputtering yields for both elements were drastically different; this affirmed the expectation that sputtering behavior varies as a function of depth in a sample. Sputtered particles originating predominantly from below the surface monolayer are more sharply peaked in angle than sputtered particles originating from the surface monolayer of the sample. Furthermore, for samples such as the Ga-In sample studied here that have the heavier constituent on the surface, the energy distribution for the atoms sputtered from beneath the surface are broader than for atoms from the surface. This may be related to the kinematics of the final collision before the ejection of each sputtered particle; this proposed mechanism would be an interesting topic for further study.

This study offers additional basic sputtering information to both the sputtering industry and to sputtering theorists. It provides more fundamental knowledge of the basic sputtering process as applied to multilayered samples. Also, this study provides experimental results of aspects of sputtering that have not been previously measured to encourage future development of sputtering theory.

Recommendations for future work involve improvements in uncertainty. An ion beam buncher design could improve the temporal uncertainty. Upgrading the tunable laser source could provide a cleaner, more efficient, and more reliable resonance ionization source. Eventually, the MCP/phosphor screen assembly may need to be replaced. And finally, a thorough characterization of the electrostatic quadrupole triplet lens for the primary ion beam is anticipated.

This study was the maiden SIRIS experiment conducted with the apparatus. A personal remark is that tremendous experience was gained in the development, construction, and implementation phases of the project. This apparatus has the capability to detect single sputtered atoms. Future applications may include continued sputtering behavior studies and impurity measurements.

REFERENCES

1. R. Behrisch (ed.): *Sputtering by Particle Bombardment I*, Topics in Applied Physics (Springer, Berlin, 1981), pp. 11-12, 15-18.

2. *Webster's Illustrated Dictionary*, (Books, Inc., New York, 1964), p. 642.

3. M. Vicanek and H.M. Urbassek, Nucl. Instr. and Meth. B **30**, 507 (1988).

4. M. Vicanek, U. Conrad, and H.M. Urbassek, Phys. Rev. B **47**, 617 (1993).

5. P. Sigmund and N.Q. Lam, Mat. Fys, Medd. Dan. Vid. Selsk. **43** (1993) 255.

6. K.M. Hubbard, R.A.Weller, D.L. Weathers, T.A. Tombrello, Nucl. Inst. and Meth. B **36**, 395 (1989).

7. R. Behrisch (ed.): *Sputtering by Particle bombardment III*, Topics in Applied Physics (Springer, Berlin, 1982), pp. 2.

8. P. Sigmund, Phys. Rev. **184** (2), 383 (1969).

9. K. Huang, Statistical Mechanics, (Wiley, New York, 1963), pp. 55-67.

10. P.Sigmund, Nucl. Inst. and Meth. B **18**, 375 (1987).

11. P.K. Haff, Appl. Phys. Lett. **31** (4), 259 (1977).

12. L. Galkute, L. Pranevi□ius and G. Zubauskas, Nucl. Inst. and Meth B **21**, 46 (1987).

13. M.J. Pellin and J.W. Burnett, Pure and Appl. Chem., **65** (11), 2361 (1993).

14. M.H. Shapiro, K. Bengtson, Jr., and T.A. Tombrello Nucl. Inst. and Meth B **103**, 2 (1995).

15. M.F. Dumke, T.A. Tombrello, R.A. Weller, R.M. Housley, and E.H. Cirlin, Surf Sci. **124**, 407 (1983).

16. K.M. Hubbard, R.A. Weller, D.L. Weathers, and T.A. Tombrello, Nucl. Instr. and Meth. B **40/41**, 278 (1989).

17. SRIM program, 1996, IBM Research, New York, USA.

18. C.D. McMillon, A.W.Bigelow, and D.L. Weathers, *Texas Section of the American Physical Society, Fall Meeting, University of North Texas, Denton, Texas, October 9-11, 1997*

19 H.F. Arlinghaus, M.T. Spaar, T. Tanigaki, A.W. McMahon, and P.H. Holloway, J. Vac. Sci. Technol. B, **12** (1), 263 (1994).

20 L.C. Feldman and J.W. Mayer, *Fundamentals of Surface and Thin Film Analysis*, (North-Holland, New York, 1986), p. 88.

21 Cockcroft-Walton accelerator manual.

22 O. Truong, A.M. Childs, A.W. Bigelow, S. Matteson, D.L. Weathers, Joint Fall Meeting of the Texas Sections of APS and AAPT, and SPS Zone 13, Lubbock, 1995.

23 A.W. Bigelow, A.M. Childs, D.L. Weathers, and S. Matteson, Joint Fall Meeting of the Texas Sections of APS and AAPT, and SPS Zone 13, Arlington, 1996.

24 S. Matteson, D.K. Wilson, D.L. Weathers, F.D. McDaniel, J.L. Duggan, and J.M. Anthony, Nucl. Inst. and Meth. B **56/57**, 1091 (1991).

25 G.S. Hurst, M.G. Payne, S.D. Kraemer, and J.P. Young, Rev. Mod. Phys. **51** (4), 767 (1979)

26 E.B. Saloman, Spectrochimica Acta **49B** 3, 251 (1994).

27 E.B. Saloman, Spectrochimica Acta **48B**, 1139 (1993).

28 Pulsed Dye Laser Manual, Spectra Physics

29 R.E. Haskell, Am. Journal of Physics **38** (8), 1039 (1970).

30 The Optics Project software, http://www.erc.msstate.edu/~foley/newtop/, Mississippi State University.

31 G.A. Somorjai, *Introduction to Surface Chemistry and Catalysis*, (Wiley, New York, 1994), pp. 12-13.

32 P.H. Kobrin, G.A. Schick, J.P. Baxter, and N. Winograd, Rev. Sci. Instrum. **57** (7), 1354 (1986).

33 S.L. Li, A.W. Bigelow, D.L. Weathers, Joint Spring Meeting of the Texas Sections of APS and AAPT, and SPS Zone 13, Abilene, 1996.

34 National Instruments, 6504 Bridge Point Parkway, Austin, TX, 78730-5039.

35. K.M. Hubbard and R.A. Weller, Surface Science **207**, 441 (1989).

36. T.B. Lill, W.F. Callaway, M.J. Pellin, and D.M. Gruen, Phys. Rev. Lett. **73** 12, 1719 (1994).

37. Alafa Aesar, Material Safety Data Sheet.

38. M.F. Dumke, T.A. Tombrello, R.A. Weller, R.M. Housley, and E.H. Cirlin, Surface Science **124**, 407 (1983).

39. H. Arkin and R.R. Colton, *Statistical Methods*, (Barnes & Noble, New York, 1956), p. 38.